CRYSTALLIZATION AND PHASE SEPARATION MECHANISM OF SILICON OXIDE THIN FILMS FABRICATED VIA ELECTRON BEAM EVAPORATION OF SILICON MONOXIDE

A THESIS SUBMITTED TO
THE GRADUATE SCHOOL OF NATURAL AND APPLIED SCIENCES
OF
MIDDLE EAST TECHNICAL UNIVERSITY

BY

DENİZ CİHAN GÜNDÜZ

IN PARTIAL FULFILLMENT OF THE REQUIREMENTS
FOR
THE DEGREE OF MASTER OF SCIENCE
IN
MICRO AND NANOTECNOLOGY

JUNE 2015

Approval of the Thesis:

CRYSTALLIZATION AND PHASE SEPARATION MECHANISM OF SILICON OXIDE THIN FILMS FABRICATED VIA ELECTRON BEAM EVAPORATION OF SILICON MONOXIDE

submitted by **DENİZ CİHAN GÜNDÜZ** in partial fulfillment of the requirements for the degree of **Master of Science in Micro and Nanotechnology Department, Middle East Technical University** by,

Prof. Dr. Gülbin Dural Ünver
Dean, Graduate School of **Natural and Applied Sciences** _____

Prof. Dr. Tayfun Akın
Head of Department, **Micro and Nanotechnology** _____

Prof. Dr. Raşit Turan
Supervisor, **Physics Dept., METU** _____

Assist. Prof. Dr. Selçuk Yerci
Co-Supervisor, **Electrical and Electronics Eng. Dept., METU** _____

Examining Committee Members:

Prof. Dr. Mehmet Parlak
Physics Department, METU _____

Prof. Dr. Raşit Turan
Physics Department, METU _____

Prof. Dr. Macit Özenbaş
Metallurgical and Materials Engineering Department, METU _____

Assist. Prof. Dr. Selçuk Yerci
Micro and Nanotechnology Department, METU _____

Assoc. Prof. Dr. Ceyhun Bulutay
Physics Department, BU _____

Date: 19.06.2015

I hereby declare that all information in this document has been obtained and presented in accordance with academic rules and ethical conduct. I also declare that, as required by these rules and conduct, I have fully cited and referenced all material and results that are not original to this work.

Name, Last Name: Deniz Cihan Gündüz

Signature :

ABSTRACT

CRYSTALLIZATION AND PHASE SEPARATION MECHANISM OF SILICON OXIDE THIN FILMS FABRICATED VIA ELECTRON BEAM EVAPORATION OF SILICON MONOXIDE

Gündüz, Deniz Cihan

M.S., Department of Micro and Nanotechnology

Supervisor: Prof. Dr. Raşit Turan

Co-Supervisor: Asst. Prof. Selçuk Yerci

June 2015, 69 pages

Silicon nanocrystals (NCs) imbedded in a matrix of silicon oxide have drawn much attention due to their applications in optoelectronic devices and third-generation solar cells. Several methods were reported for the fabrication of Si NCs. Among these techniques, there are aerosol synthesis, chemical vapor deposition, ion implantation, magnetron sputtering and thermal evaporation. However, electron beam evaporation is a straightforward and effective technique for the fabrication of silicon oxide thin films since it allows a broad range control of evaporation rate.

In most of the studies regarding electron beam enabled fabrication of silicon oxide thin films, co-evaporation of Si and SiO_2 was employed. However, SiO is a less studied compound and the structure of commercially available SiO materials is still an issue of debate. Some studies characterized commercially available SiO materials as a mixture of Si and SiO_2 rather than silicon (II) oxide.

In this work, silicon oxide thin films were synthesized via e-beam evaporation of SiO. A broad range of annealing times and temperatures were spanned. Raman spectroscopy, XPS and FTIR were employed to study the mechanism of crystallization

and phase separation of films. Raman spectroscopy results show that SiO cannot be considered as a composite mixture of Si and SiO_2. Results indicate that phase separation and crystallization are two separate processes even at high temperatures. A minimum annealing temperature of between 800 and 900^0 C is required to form Si NCs in this kind of a Si-O system. A complete crystallization of films was observed at 1200^0 C.

Key Words: *SiO, phase separation, crystallization, electron beam (eb) evaporation.*

ÖZ

ELEKTRON DEMETİ BUHARLAŞTIRMAYLA ÜRETİLMİŞ SİLİSYUM OKSİT İNCE FİLMLERİN KRİSTALLENME VE FAZ AYRIŞMASI MEKANİZMASI

Gündüz, Deniz Cihan

Yüksek Lisans, Mikro ve Nanoteknoloji Bölümü

Tez Yöneticisi: Prof. Dr. Raşit Turan

Ortak Tez Yöneticisi: Yrd. Doç. Dr. Selçuk Yerci

Haziran 2015, 69 sayfa

Silisyum oksit malzeme içine gömülü silisyum nanokristallerin opto-elektronik gereçler ve üçüncü nesil güneş gözelerindeki kullanımı büyük bir ilgi odağına haline gelmiştir. Silisyum nanokristallerin üretiminde çeşitli yöntemler rapor edilmiştir. Bu yöntemler arasında aerosol sentezlemesi, kimyasal buhar biriktirme, iyon implantasyonu, magnetron saçtırma ve termal buharlaştırma bulunmaktadır ancak elektron demeti buharlaştırma buharlaşma hızının geniş bir yelpazede kontrolünü sağladığı için silisyum oksit ince filmlerin üretilmesinde kolay ve etkili bir yöntemdir.

Elektron demeti buharlaştırma etkin silisyum oksit ince filmlerin üretimi çalışmalarının çoğunda Si ve SiO_2 birlikte buharlaştırması kullanılmıştır. Ancak, SiO daha az çalışılan bir bileşiktir ve piyasadaki mevcut SiO malzemelerin yapısı hala tartışma konusudur. Bazı çalışmalar piyasadaki mevcut SiO malzemeleri silisyum (II) oksit yerine Si ve SiO_2 karışımı olarak karakterize etmiştir.

Bu çalışmada silisyum oksit ince filmler SiO'nun E-demeti buharlaştırmasıyla sentezlenmiştir. Tavlama süreleri ve sıcaklıkları geniş bir yelpazede tarandı. Raman spektroskopisi, XPS ve FTIR filmlerin kristalizasyon ve faz ayrışması mekanizmasını çalışmak için kullanılmıştır. Raman spektroskopisi sonuçları SiO'nun Si ve SiO_2'nun kompozit karışımı olarak görülemeyeceğini göstermektedir. Sonuçlar faz ayrışması ve kristalizasyonun yüksek sıcaklıklarda bile iki ayrı süreç olduğunu göstermektedir. Bu tür bir Si-O sisteminde silisyum nanokristalleri oluşturmak için gereken en düşük tavlama sıcaklığı 800^0 C ve 900^0 C arasındadır. Filmlerin tam kristallenmesi 1200^0 C'de gözlenmiştir.

Anahtar Kelimeler: *SiO, faz ayrışması, kristallenme, electron demeti (ed) buharlaştırma.*

to my dearest family…

ACKNOWLEDGEMENTS

First and foremost I would like to express my deepest gratitude to my supervisor, Professor Raşit TURAN, director of The Center for Solar Energy Research and Applications, for providing me the opportunity to be a member of his research group. I will always be grateful to him for his endless support, excellent guidance and encouragement.

I would also like to thank my co-advisor, Assistant Professor Selçuk Yerci, for his fruitful discussions. He has been always close to listen and give advice.

I would like to thank Prof. Mehmet Parlak for his help and support. I am thankful to Associate Professor Alpan Bek for his informative discussions on Raman spectroscopy results.

At the beginning of my studies, I started working together with Dr. Mücahit Yılmaz before he left. He always showed a pleasant personality, helped and supported me. Dr. Aydın Tankut's comments, discussions and valuable suggestions on my research helped me a lot. Working with him was a precious experience for me. I am also thankful to my colleagues Salar Sedani and Mehmet Karaman for their efforts to keep e-beam system working and their contributions to thin film synthesis processes.

I would also like to thank all Günam members: Dr. Tahir Çolakoğlu, Fırat Es, Hisham Nasser, Musa Kurtuluş Abak, Hande Çiftpınar, Serra Altınoluk, Olgu Demircioğlu, Gülsen Baytemir, Zeynep Demircioğlu, Yasin Ergunt, Dr. Engin Özkol, Mona Zolfaghariborra, Mete Günoven, Özden Balbaşı, Beran Acar, Umut Çaçan, Anıl Şeker, Buket Gökbakan, Tuncay Güngör, technician Yücel Eke, technician Nevzat Görmez, technician Dursun Erdoğan, technician Tayfun Yıldız.

I would like to thank the Scientific and Technical Research Council of Turkey (TUBITAK) for financial support during my master study.

I am thankful to thesis committee members.

I finally thank to my family for their support and encouragements.

TABLE OF CONTENTS

LIST OF FIGURES

FIGURES

LIST OF TABLES

TABLES

CHAPTER 1

INTRODUCTION

1.1. Silicon Technology

There is not any other technological area influencing the life of ordinary people as much as silicon technology. Almost in each part of our lives, we feel the effects of this technology since our lives are imbued with it from television to computers. It does not only affect the everyday life of people but it also shapes the lives via changing the habits and cultures with its strong power. For example, the effects of internet on social movements is a popular discussion subject in sociology nowadays. In addition to social effects, silicon technology has major role in industry and military powers of countries. It is expected that silicon technology will keep its strong position through many years.

Considering the evolution of electronics, main elements of electronics were vacuum tubes and copper wires at the beginning. Currently, it is possible to produce a single silicon chip, an example is given in Figure 1, which has more than a billion transistors and copper interconnections. Photonics is the potential area to provide the long term solution. For the case of optical interconnect schemes, system of lasers, modulators, optical waveguides and photo-detectors can take the place of the copper wires between integrated circuits. This could give the opportunity to get rid of the cross talk, power loss in signal propagation and delay. On the other hand, probably new potential challenges will arise for signal detection.

To increase the performance of chips, researchers focused on increasing transistor channel width so as to reach greater drive currents. This can result in transistor-level circuit. This attempt was quite basic. On the other hand, the main problem, which is electrical performance of wires or metal interconnections, was ignored for a long time.

The latency in interconnects and energy loss are the main barriers in front of the transistor performance.

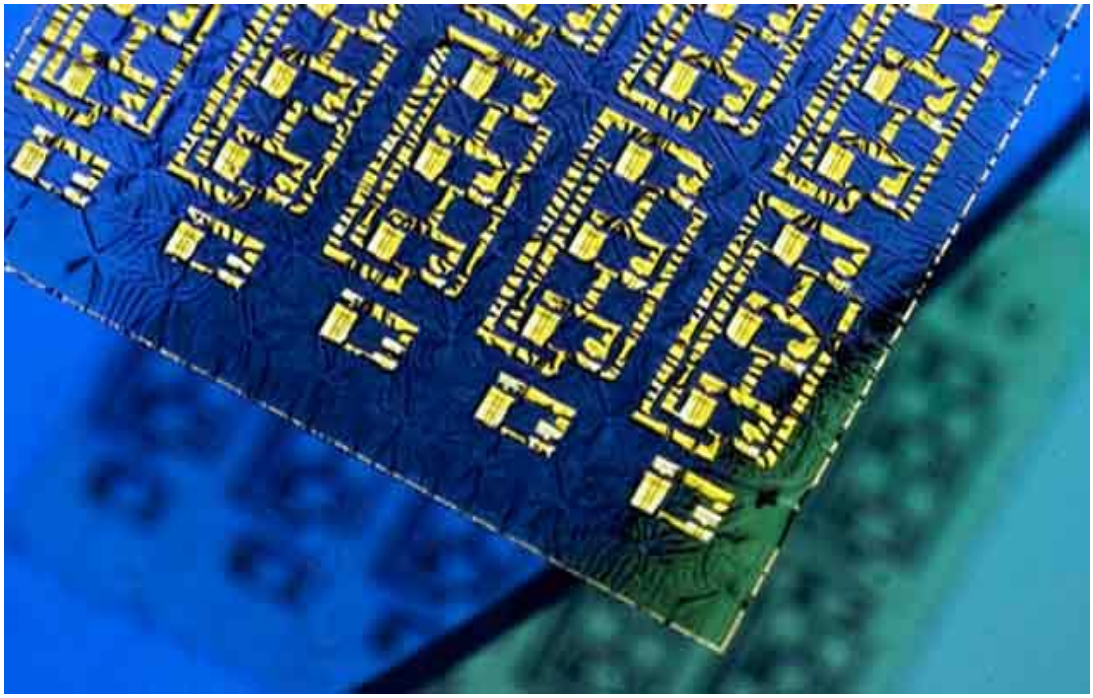

Figure 1: An example of a silicon integrated circuit [1].

Great performance improvements is not the only success story in silicon technology. The manufacturing costs for each component exponentially decreases while keeping their performance level. The very famous observation "Moore's law" states that, the amount of transistors in a dense integrated circuit doubles almost every two years. This observation is named after Gordon E. Moore, who is co-founder of the Intel Corporation, whose paper showed a doubling each year in the amount of components per integrated circuit in 1965 [2] [3] [4].

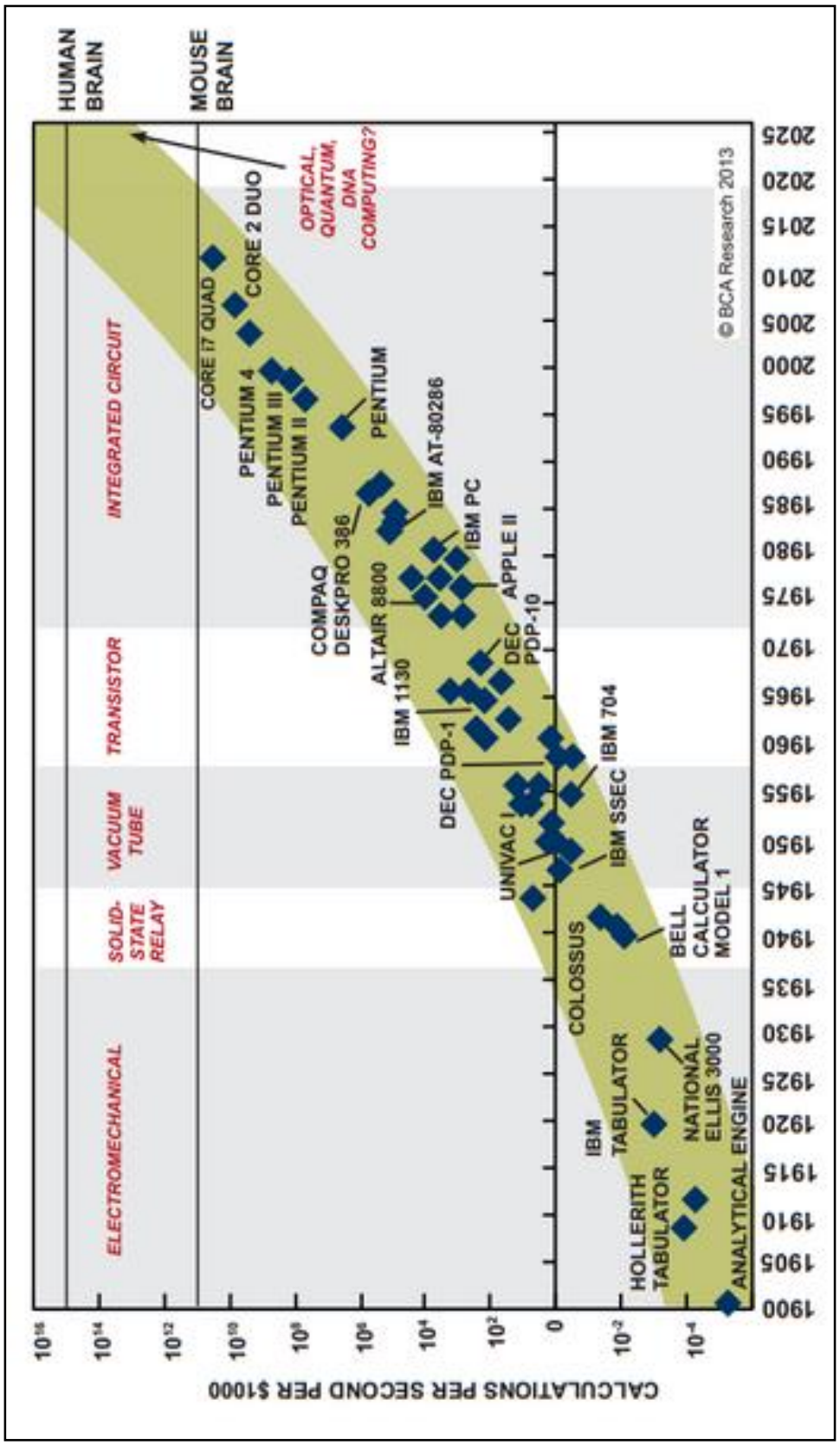

Figure 2: CPU transistor counts versus introduction dates [60].

Referring to Figure 2, Moore's law maintains its significance nowadays. With the great advance in the technology, it became quite cheaper over time to put much more transistors into integrated circuits due to the fact that transistors are getting smaller in size. The great advance in scale aspect made it possible to produce better chips with more transistors almost in the same prices. The possibility of making smaller transistors also resulted in a decrease in the price of old generation chips because of the fact that better chips can be produced on silicon wafer for similar prices.

1.2. Silicon Photonics

Silicon photonics is the area of research and application of photonic systems which silicon is used as an optical medium [5] [6] [7]. Researchers working in the area of silicon photonics aim to fabricate high performance optical devices via using CMOS compatible material sources. CMOS is the short name for Complementary Metal Oxide Semiconductor. The power efficiency of CMOS circuits make them the most significant candidate to be used in microprocessors. CMOS is also used in microcontrollers, Random-access memory, and logic circuits. Moreover, it can also be used for CMOS sensor (Figure 3), data converters and integrated transceivers. In institutions where CMOS production is taking place, necessary precautions are taken not contaminate these CMOS materials. Generally, the main problems in silicon photonics lie under material integration and production issues.

Silicon is also candidate material for photonics thanks to its CMOS compatibility. The high index of refraction, thermal conductivity and mechanical strength of silicon put it as the first material in electronics industry. Those qualities are also valuable for photonics. On the other hand, silicon is a not a valuable material to be used in the production of making lasers. In addition to this, silicon also bad candidate to be used in the production of light emitting devices, since the band gap of silicon is indirect. In order to overcome aforementioned obstacles nano-sized silicon structures offer new possibilities via their tunable band gap.

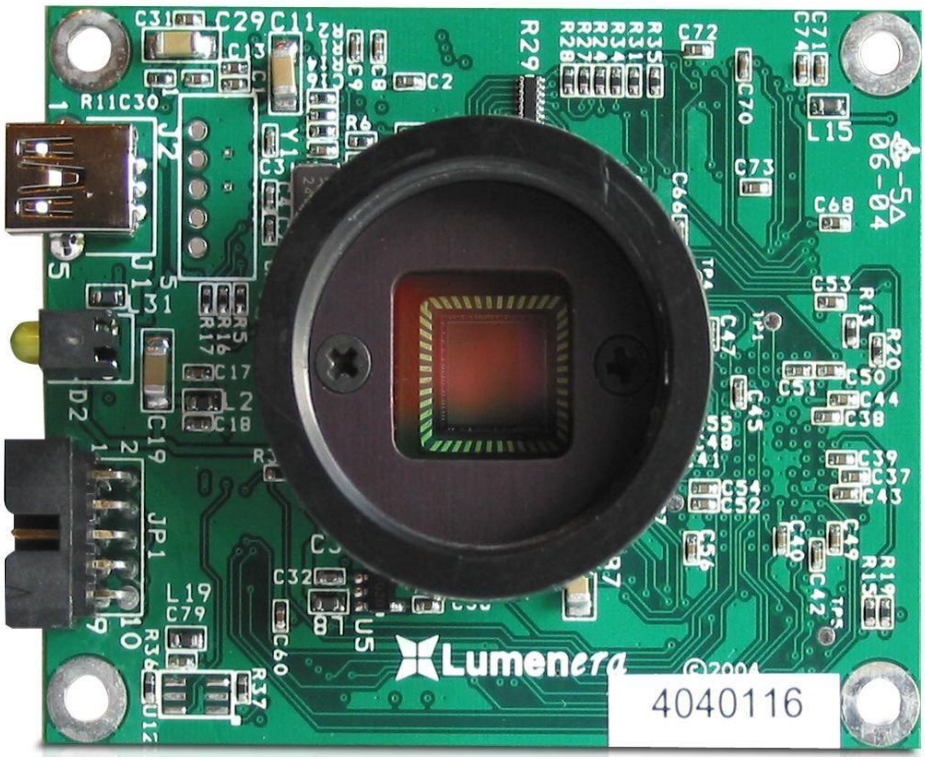

Figure 3: A commercially available CMOS board camera based on CMOS sensors [8].

1.3. Silicon Photovoltaics

History of photovoltaics can be dated back to the discovery of photovoltaic effect by William Grylls Adams and his student, Richard Evans Day, while they were doing experiments on an electrolytic cell made up of two metal electrodes in 1839. In spring 1953, while carrying out research on silicon for its electronic applications, Gerald Pearson, an experimental physicist at Bell Laboratories, accidentally made a photovoltaic cell. Daryl Chapin and Calvin Fuller, also experimental physicists at Bell Laboratories, did some changes on Pearson's solar cell and made the first solar cell with an efficiency of 6% that can convert enough of the solar energy to power to be used in electrical equipment [9].

At 2015, silicon is still the key material for photovoltaics. Silicon is used in solar cells (Figure 4) as the starting material of monocrystalline and multicrystalline and also of

thin film silicon modules. Nearly 90% of the annual solar cell production is based on silicon. The cost per Wp (Wp, peak power under standard test conditions) by the direct conversion of solar energy to electrical power via use of wafer based solar cells decreased and the conversion efficiency increased due to the better understanding the conversion limiting factors.

There is no resource limitation silicon photovoltaics and currently solar cell efficiencies are greater than 18% for multicrystalline and 20% for single crystal. Even for current values silicon photovoltaics is a successful technology. On the other hand, there are many possible improvements that can be achieved in the future, which can guarantee the role of silicon photovoltaics in world energy market.

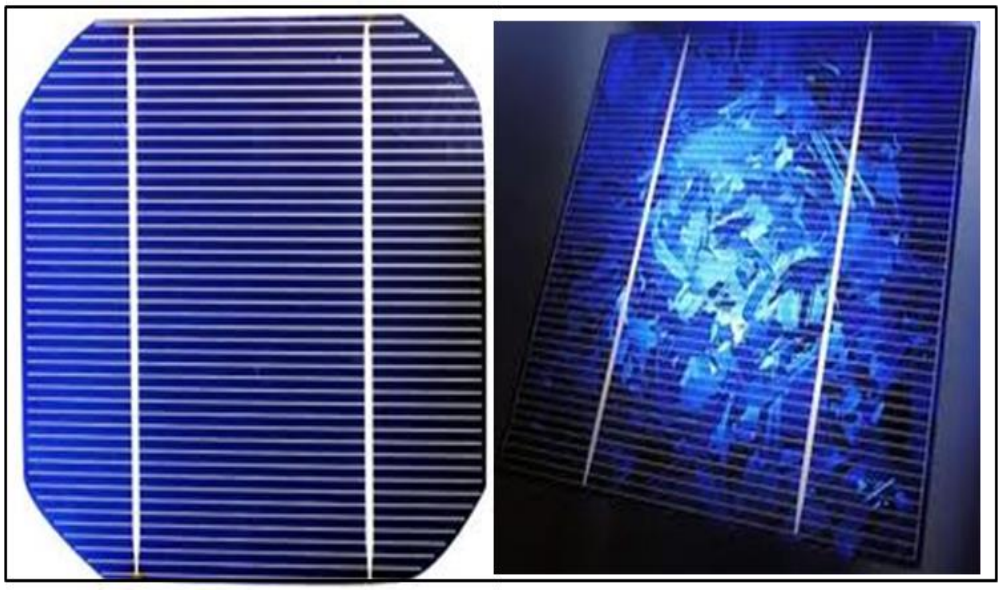

Figure 4: Industrial mono and multi crystalline silicon solar cells [10].

Because of the fact that the bandgap of silicon nanocrystals can be tuned, the solar spectrum can be effectively absorbed via silicon nanocrystals with bandgaps and different sizes in the same solar cell device, which is not possible in classical ways. This can lead to the fabrication of solar cell devices with higher efficiencies.

1.4. Silicon Nanocrystals

As previously mentioned in Silicon Photonics section, silicon is not a good candidate to be used in the light emitting devices because of its indirect band gap. The solution to this problem is to make use of quantum mechanical effects so as to yield better optical properties. In general nanostructured silicon and especially silicon nanocrystals are significant candidates to be used in silicon photonics.

The first experimental results showing optical emission in nano-sized silicon was obtained from porous silicon, which has been produced via electrochemically etching silicon [11]. After the first observation, optical emission from nanostructured silicon materials via different fabrication techniques has been reported. Among these techniques, there are aerosol synthesis [12], ion implantation [11] [14], laser ablation [15], chemical vapor deposition (cvd) of sub-stoichiometric oxide films [16] [17], magnetron sputtering [18] and thermal evaporation of Si-rich oxides [19]. In all of the abovementioned examples, quantum mechanical properties are responsible for the desired effects.

The quantum mechanical effects can also play a significant role in silicon photovoltaics. Multijunction photovoltaic cells that have stacked p–n junctions formed via silicon nanocrystals with different sizes have been designed with a theoretical efficiency values exceeding 50% [20].

The enhancement in the photonic and photovoltaics properties of materials are due to quantum mechanical effects. Despite the fact that the laws of classical mechanics is valid for macro systems, they fail in length scale of the de Broglie wavelength. The length scale of the de Broglie wavelength is on the order of nanometers. Therefore,

electrons are also in the de Broglie wavelength size regime, quantum mechanical effects can be exploited to produce quantum devices. The quantum confinement effect which is responsible for changes in the electrical, optical and mechanical properties of materials can be explained via simple particle in a box problem, which will be discussed in details in theory section.

1.5. Thesis Objective

In spite of the fact that there are several aforementioned techniques for the fabrication of Si NCs, electron beam (EB) evaporation is a straightforward and effective technique for the fabrication of silicon oxide thin films since it allows a broad range control of evaporation rate.

In most of the studies regarding electron beam (EB) enabled fabrication of silicon oxide thin films, co-evaporation of Si and SiO_2 was employed. Si is the material all the modern technology based on. SiO_2 is one of the most abundant and studied compounds on earth [21] [22]. Its prominence is because of its role in geophysics and geochemistry of the Earth and other planets and its broad range of applications from photovoltaics to catalysis.

Si NCs can also be fabricated via disproportionation reaction of silicon monoxide, SiO. On the other hand, silicon monoxide is a less studied compound and the structure of commercially available solid silicon monoxide materials is still an issue of debate. Some studies characterized commercially available solid silicon monoxide materials as a mixture of Si and SiO_2 rather than silicon (II) oxide [23] [24].

Up to now, there is no detailed study investigating a broad range of annealing times and temperatures to reveal crystallization and phase separation mechanism of thin films deposited via SiO target. This study investigates whether SiO can be considered as a mixture of Si and SiO_2 and spans a broad range of annealing times and temperatures to reveal crystallization and phase separation mechanism of thin films deposited via electron beam (EB) evaporation of SiO target.

CHAPTER 2

THEORY

2.1. Quantum confinement

Quantum confinement effect appears when the diameter of a material is around the magnitude as the de Broglie wavelength of the charge carriers. Once materials are this much small, severe changes in their electronic and optical properties take place [25].

Once the confining dimension is greater than the de Broglie wavelength of the particle, it behaves as a free particle. No change in the bandgap of particle takes place since there is no change in its original energy because of a continuous energy state. On the other hand, after the confining dimension gets smaller and reaches a sufficiently small size, which is a certain limit, typically 10 nanometers or less, the energy spectrum becomes discrete. As a result of that, the bandgap depends on size of particle.

An exciton is made up of an electron and a hole. In a more specific point of view, the quantum confinement effect arises once electrons and electron holes are being squeezed into a dimension that goes to a critical length, known as the exciton Bohr radius. Then, the energy levels in nanocrystals are quantized because of the confinement of electrons and energy states of the electron and hole become size dependent. As the size of nanocrystals become smaller, the difference between energy states gets larger. Because of the fact that the optical and electrical properties depend highly on band gap, necessary optical and electrical structures can be fabricated according to the needs via making use of quantum confinement effect.

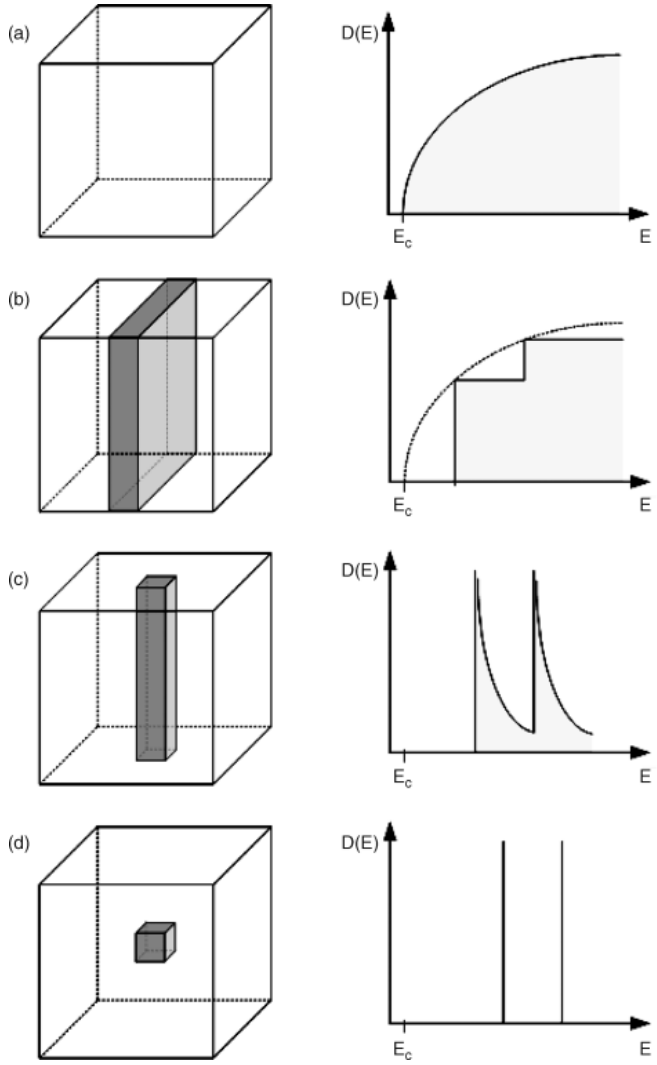

Figure 5: Diagram of effect of electronic confinement on the density of states in semiconductor structures with different dimensionalities (a) bulk (b) one-dimensional confinement in a quantum well, (c) two-dimensional confinement in a quantum wire, and (d) three-dimensional confinement in a quantum dot [26].

As experimental examples, a nanocrystal, which can be assumed as a small sphere confines electrons in three dimensions, a quantum wire confines electrons in two dimensions, and a quantum well confines electrons in one dimension. A schematic of effect of electronic confinement on the density of states is given in Figure 5. These

examples can also be named as zero-, one- and two-dimensional potential wells in a respective order. Those dimensions stands for the fact that confined particles can act as a free particle in that abovementioned dimensions.

The quantum confinement in nanocrystals can be modeled via use of effective mass approach. In this model, electrons and holes with isotropic effective masses in a three-dimensional potential well which is a spherical potential box with an infinite potential is considered. The main energy terms are the confinement energy of the electron and hole and the Coulomb interaction between electron and hole. Nanocrystals are in the weak confinement regime for the case that their radii are on the approximate order of the exciton Bohr radius. On the other hand, nanocrystals are in the strong confinement regime once their radii are much smaller than the exciton Bohr radius.

For the case of weak confinement regime, exciton Bohr radius is equal to the sum of the electron and hole radii. In this case the dominant energy term is the coulomb term. Motion of the exciton is subject to size quantization. The minimum energy state is the exciton state whose energy is shifted to greater energies due to confinement, where the shift in energy is proportional to $1/R^2$. The energy shift of the minimum energy state of exciton can approximately be expressed as in the following equation:

$$\Delta E \approx \frac{h^2 \pi^2}{2MR^2} \qquad (Eq.1)$$

Where M is the mass of the exciton, calculated via the sum of effective masses of electron and hole.

For the case of strong confinement regime, the electron and hole interaction energy (the Coulomb term) term is small; therefore, can be ignored or seen as a perturbation. Because of the fact that the excitons are not formed, electrons and holes can be considered as independent particles. As a result, size quantization of the electron and hole are separate events. The energy shift of the minimum energy state can approximately be shown as in the following equation:

$$\Delta E \approx \frac{h^2\pi^2}{2\mu R^2} \qquad (Eq.2)$$

Where the exciton mass M is replaced via the reduced exciton mass, μ which can be expressed as:

$$\frac{1}{\mu} = \frac{1}{m_e^*} + \frac{1}{m_h^*} \qquad (Eq.3)$$

With m_e^* and m_h^* are the effective masses of the electron and hole in a respective order [27].

2.2. Classical Nucleation Theory

On the formation of a new thermodynamic phase or a new structure via self-assembly or self-organisation, nucleation is the first step. The process that determines how much times required before the genesis of new phase or self-organised structure is defined as nucleation. The most general theoretical model used to explain the mechanism of nucleation is classical nucleation theory. Mechanism of nucleation is the answer to the questions such as why nucleation may take minutes, hours or in some cases years, or actually never happen [28] [29] [30].

Classical nucleation theory is a standard simple approximate theory. For nucleation of a new phase, the basic classical nucleation theory gives an approximate but physically reasonable prediction for phase formation rate, via assumption of identical nucleation sites. Phase formation rate, R, can be expressed as in the following equation:

$$R = N_S Z j \exp\left(\frac{-\Delta G^*}{k_B T}\right) \qquad (Eq. 4)$$

Where ΔG^* is the free energy of the nucleus at the top of the nucleation barrier, $k_B T$ is the thermal energy, T is the absolute temperature and k_B is the Boltzmann constant. N_S is the amount of nucleation sites and j is the rate of attachment of molecules to the nucleus leading to an increase in the size of the nucleus.

Lastly, Z is the Zeldovich factor. Zeldovich factor stands for the probability that a nucleus at the top of the barrier starts the formation of a new phase rather than dissolving.

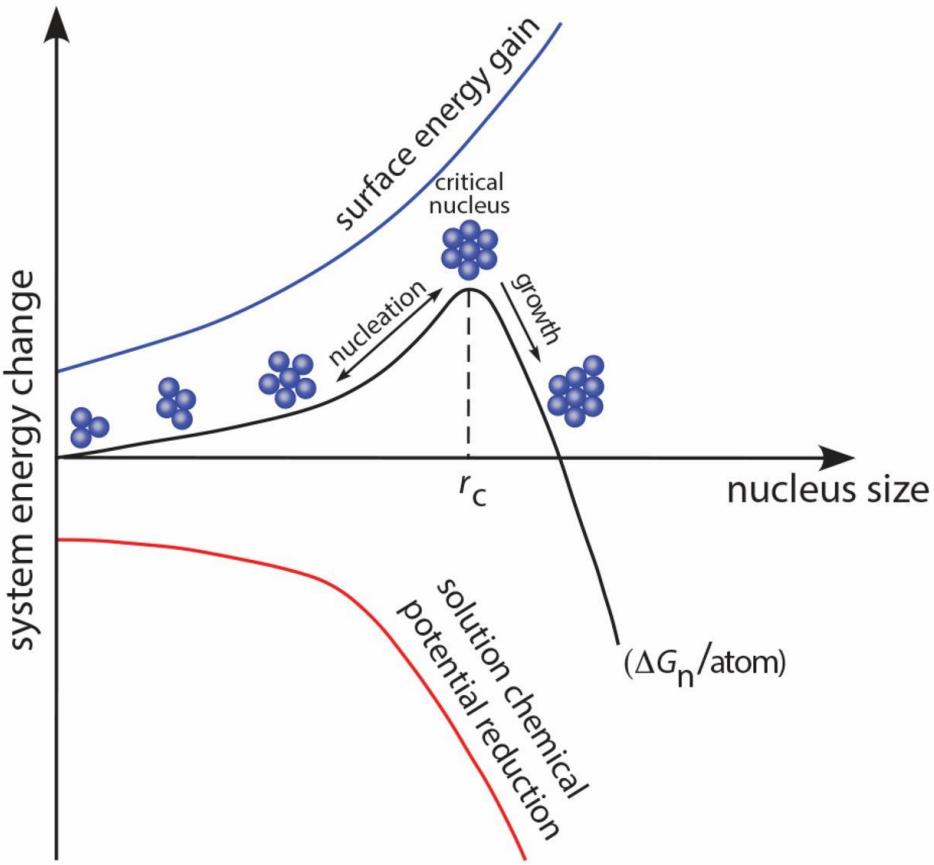

Figure 6: System energy change as a function of nucleus radius [31].

In Figure 6, the black curve is the cumulative free energy as a function of radius. This is called as the Gibbs free energy if pressure is constant around the environment. Cumulative free energy is a sum of two terms as given in equation 2. The first is the bulk term that is plotted in red. The second term, the one due to the interface is shown with blue color.

Nucleation barrier, $\Delta G(r)$, must be calculated to find out whether nucleation is fast or slow. It is an assumption of the classical theory that even for a very small nucleus of the new phase, the free energy of a droplet ΔG can be written as the sum of a bulk term

which is proportional with the nucleus volume; and a surface term, which is proportional to its surface area as given in the following equation:

$$\Delta G = \frac{4}{3}\pi r^3 \Delta g + 4\pi r^2 \sigma \qquad (Eq.5)$$

Where the first term in the right hand side of the equation is the volume term, and with the assumption that nucleus is spherical, this term is the volume of a sphere of radius r. Δg is the free energy difference for unit volume between the thermodynamic phase nucleation is taking place in, and the phase which is nucleating. As an example, if crystalline silicon is nucleating in amorphous silicon, then Δg is the free energy per unit volume of the amorphous silicon minus that of crystalline silicon. The second term in the right hand side of the equation is due to the interface at surface of the nucleus, that is also the reason why it is proportional to the surface area of a sphere. σ is the surface tension at the interface between the nucleus and its surrounding area. σ is always positive [32].

2.3. Particle Coarsening: Ostwald Ripening

Ostwald ripening is an observation in solid solutions or liquid sols which is used to describe the evolution of an inhomogeneous structure over time such that small crystals or sol particles transform into larger crystals or sol particles [33]. The physical phenomenon is named after its discovery by Baltic German chemist Wilhelm Ostwald in 1896 [34]. Ostwald ripening is actually phase transformation process that has been observed in various systems such as metallic and nonmetallic systems where there are particles with different sizes in a matrix. The driving force of this process is that larger

particles are more energetically favored than smaller particles. This is due to the fact that molecules on the particle surface are energetically less stable than the ones in bulk.

At all the stages of Ostwald ripening, there is an important parameter called as critical particle radius, R*. Particles having the same radius with critical particle radius are in equilibrium with the mean matrix composition. On the other hand, particles having a radius greater than critical particle radius will continue to grow and particles having a radius smaller than critical particle radius will shrink.

There has been many theoretical attempts to quantitatively model Ostwald Ripening [35]. In 1958, Lifshitz and Slyozov did a statistical analysis of Ostwald ripening for the case where diffusion of material is the slowest process [36]. The initial point they focused on was the question how a single particle grows in a solution. The final equation they come up with is as follows:

$$< R >^3 - < R >_0^3 = \frac{8\gamma c_\infty v^2 D}{9R_g T} t \qquad (Eq. 6)$$

Where $< R >$ is average radius of all the particles, $< R >_0$ is the original mean particle size at onset of coarsening γ is particle surface tension or surface energy, c_∞ is solubility of the particle material, v is the molar volume of the particle material, D is the diffusion coefficient of the particle material, R_g is ideal gas constant, T is absolute temperature and t is time.

This equation describes the case where the boundary is between small, shrinking particles and large, growing particles. They finally concluded that the average radius of the particles ⟨R⟩, grows.

Carl Wagner published his own mathematical approach on Ostwald ripening three years later than Lifshitz and Slyozov. In the systems that he has investigated, diffusion and both attachment and detachment at the particle surface was slow [37]. His approach and his calculations were different. However, the results he obtained was the same as the one that Lifshitz and Slyozov found for slow-diffusion systems.

CHAPTER 3

EXPERIMENTAL PROCEDURES FOR FABRICATION AND CHARACTERIZATION OF SILICON OXIDE THIN FILMS

3.1. Electron Beam Evaporator System

In chemical vapor deposition techniques, molecular gas species enters into reaction at a film surface for the genesis of the film. On the other hand, in the case of physical vapor deposition, films are deposited from sources in the form of atoms or clusters. Therefore, there is not any surface reaction taking place for the film formation.

Figure 7: Photograph of electron beam evaporator system at GÜNAM.

There are two main categories for physical vapor deposition techniques, which are evaporation and sputtering. In the case of evaporation systems, generally there is a heating source like laser beam, electron beam, thermally heated crucible, etc. for the evaporation of materials. Determination of the evaporation source depends on the material.

In this thesis study, we used electron beam evaporation technique so as to deposit SiO_x thin films via evaporation of silicon monoxide. Despite the fact that the evaporation of silicon monoxide is a straightforward technique for the fabrication of SiO_x thin films, the studies published on this subject is quite rare.

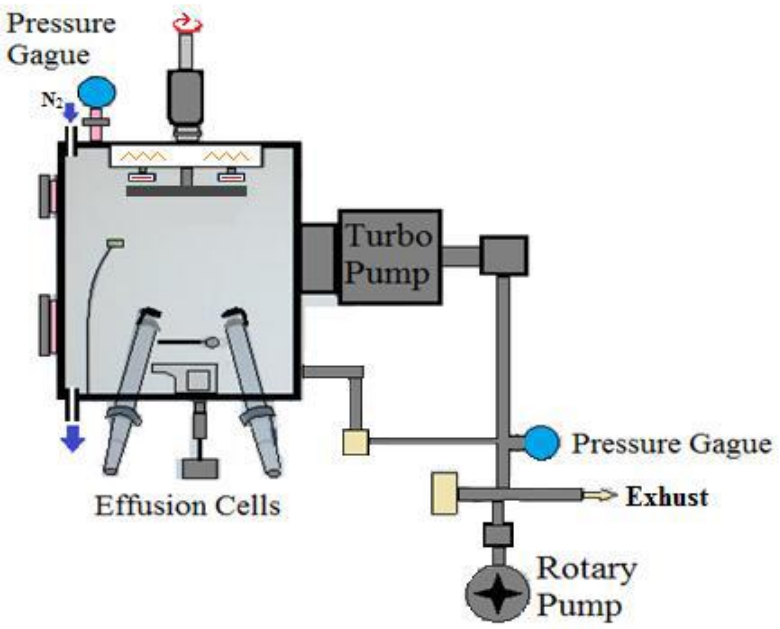

Figure 8: Schematic diagram of electron beam evaporator system at GÜNAM.

A photograph and a schematic diagram of the electron beam evaporator system at GÜNAM is given in Figures 7 and 8, respectively. E-beam evaporation is an attractive and effective way in order to evaporate a source material for thin film coatings on a substrate in standard silicon integrated circuit technology and photovoltaics. There are several main advantages of e-beam evaporation. It allows a broad range control of evaporation rate. In addition to this, using a cooled crucible allows us to eliminate film contamination, which originates from the reaction in between target and crucible. Via using e-beam evaporation, most of the materials can be evaporated, and moreover, it is possible to fabricate hydrogen-free thin films, which is quite prominent in device applications where there is a limitation of H- and N-related impurities.

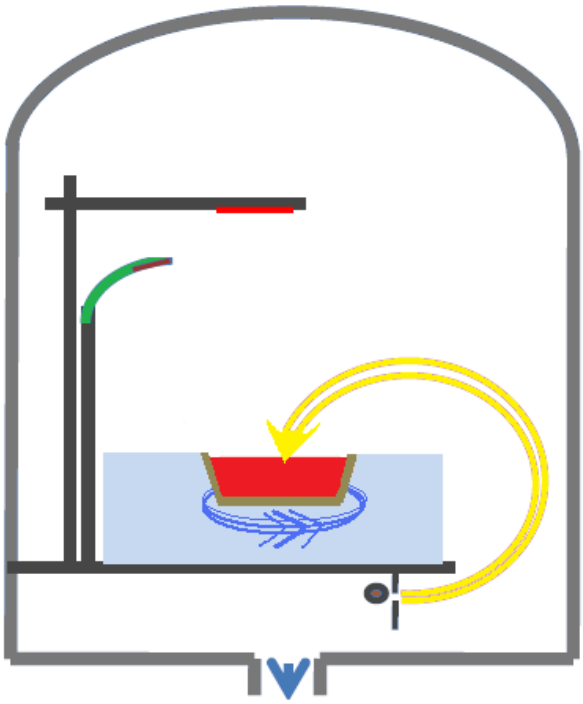

Figure 9: Schematic diagram for the working mechanism of electron gun.

In the electron beam evaporation system, the SiO target is heated via an electron beam. The genesis of those electrons takes place in a filament source. A static magnet and an electrostatic electric field generator creates an electromagnetic field, which leads to the acceleration and focusing of electron beam on to the SiO target. The working mechanism is given in Figure 9.

3.2. Selection of Substrate and Substrate Cleaning

Quartz substrates and p-type Si wafers in [100] crystallographic direction and were used during the experiments. After cutting them in suitable dimensions, they were cleaned.

Cleaning is a significant part for the fabrication of desired material. Quartz substrates used in this thesis study were cleaned via using a series of processes. The chemical processes and washing consisted of sonication in pure acetone, isopropanol and deionized water in the respective order for 10 min for all steps. After the cleaning process, substrates were dried with nitrogen gun.

For the cleaning of Si wafers, an additional initial hydrofluoric acid (HF) etching process was added for the removal of oxide layer at the top. This process is carried out via dipping of sample in 0.3 molar HF solution for 5-10 seconds.

3.3. Deposition Process of SiO_x thin films and Parameters

3.3.1. Base Pressure and Deposition Temperature

The deposition chamber was pumped down to a base pressure of $1x10^{-7}$ Torr before the deposition processes for each deposition process.

There is a pair of ceramic covered heaters which is positioned just behind the stainless steel substrate holder. Therefore, it is possible to make depositions at different temperatures. In this thesis study, depositions have been carried out at room temperature (RT) and at high temperature (HT), 400 °C.

3.3.2. Deposition Rate and Film Thickness

Deposition rate is a significant parameter for film structure. There is a direct correlation between the e-beam current used to heat the target material and deposition rate. Hence, the deposition rate can be controlled via the e-beam current. It is possible to control the rate of deposition within the range of 1 nm/sec to 50 nm/sec. The electron gun was fixed at 8.5 kV during the evaporation process. Two of the process variables can affect the deposition process, which are the e-beam current density and the spot size. The limit of e-beam current is 230 mA. In this study, 430 nm thick thin films were fabricated.

3.4. Standard Furnace Annealing

In the standard furnaces, tubes are is heated up via resistive coils. It is possible to provide high purity nitrogen gas flow through the tubes for the passivation of the annealing environment. An exemplary schematic is given in Figure 10.

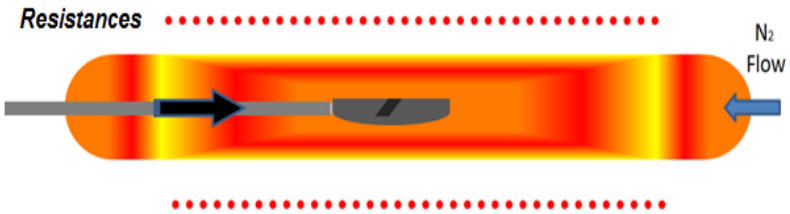

Figure 10: Schematic representation of a standard furnace with temperature gradient.

Temperature of the furnaces situated at The Center for Solar Energy Research and Applications can be adjusted manually. Samples are put into a quartz boat which is then placed into the tube furnace.

3.5 Material Characterization

3.5.1. Raman Spectroscopy

Once light passes through a molecule, the dominating mode of scattering is Rayleigh scattering. That is an elastic process, which means that the kinetic energy of incoming particle is conserved in the center-of-mass frame; however, propagation direction is changed. Hence, the wavelength does not change during the process. The amount of scattering is directly correlated with the wavelength; it is proportional with the fourth power of the frequency. Therefore, scattering becomes more effective at shorter wavelengths. When incident photons undergoes into an interaction with molecules either gaining or losing energy, a frequency shift takes place in photons. This inelastic scattering is named as Raman scattering after Indian physicist C. V. Raman who discovered the effect in 1928 [38].

Raman scattering is dependent on the polarizability of the molecules. It is possible to excite vibrational modes of the polarizable molecules via the incident photon energy, resulting in scattered photons. The energy of those photons decreases an amount corresponding to the vibrational transition energies. If the molecule is excited from a ground to a virtual state and then goes back down to a vibrational state having greater energy then the initial one, then the scattered photon has lower energy than the incident photon, and therefore has a longer wavelength. A spectral study of the scattered photons gives spectral satellite lines below the Rayleigh scattering peak at the incident frequency. These lines are known as "Stokes lines" and the scattering is named as “Stokes scattering”. Scattering frequencies higher than the incident photon frequency can also be observed if there is significant excitation of vibrational excited states of the molecules once the vibrational energy is added to the incident photon energy. These lines, which are usually weaker, named as “anti-Stokes lines” and the process is called as “anti-Stokes scattering”. In Raman spectra, as usual, Stokes peaks are displayed because anti-Stokes peaks are weaker than the Stokes peak [39].

The dipole polarization excited in solids when a laser (amplitude E_0; frequency ν_{las}) interacts with phonons (of frequency ν_{vib}) depends on the polarizability tensor α:

$$\boldsymbol{P} = \boldsymbol{\alpha} \times \boldsymbol{E_0} \cos(2\pi V_{las}\, t) \qquad (Eq.7)$$

Where polarizability tensor α can be written as individual functions of the normal vibration coordinates Q via using a Taylor approximation:

$$\alpha_{iJ} = \alpha_{iJ}{}^{0} + (\partial a_{iJ} / \partial Q)_{Q=Q_0} \times Q \qquad (Eq.8)$$

Where i and j stands for the x, y and z coordinates,

$$P_i = \sum \alpha_{ij} \times E_j \qquad (Eq.9)$$

$$P_i = \sum_j [\alpha_{ij}{}^0 \times E_{0j} \times \cos(2\pi V_{las}\, t) + \frac{E_{0j} \times Q_0}{2} \left(\frac{\partial a_{ij}}{\partial Q}\right)_{Q=Q_0} \times [cos\,(2\pi(V_{las} - V_{las})t) + cos\,(2\pi(V_{las} + V_{las})t)\,] + \ldots \qquad (Eq.10)$$

In the predictions of equation 10, there are both quasi-elastic ($\nu \sim \nu_{las}$) and inelastic ($\nu = \nu_{las} \pm \nu_{vib}$) light scattering. The first one is Rayleigh scattering while the other one is Raman scattering, which takes place once vibrations change polarizability.

From equation 10, there are two factors affecting the Raman spectra. The α_{ij} term is related to the electrical properties while the ν_{vib} term is related to the mechanical properties material. Mechanical parameters such as, strength of bonds, distances between atoms and substitution of determines the peak positions. Electrical parameters such as ionic and covalent bonds and band structure determines the peak intensity.

For the case of crystals, there are certain energies for local bonds. Since the bonding energies are narrowly distributed, there are narrow lines in Raman spectra. On the other hand, for the case of amorphous structures, bonding energies are widely distributed, thus; there are broad scattering signal for this kind of disordered structures.

Vibration modes generally referred by their wavenumber, $\bar{\nu}$, rather than frequency, ν_{vib}. Although frequency is the number of vibrations per second, wavenumber is the number of waves per centimeter. They can be expressed in terms of each other as shown in the following equation:

$$\bar{\nu} = \frac{\nu_{vib}}{c} \qquad (Eq.11)$$

where c is the speed of the light in vacuum and approximately equal to 2.99x10^8 m/s. Frequency, v_{vib}, and wavenumber, $\bar{v}$, is inversely proportional to the wavelength (λ):

$$v = \frac{c}{\lambda} \qquad (Eq. 12)$$

Where the unit of wavenumber is inverse centimeter (cm^{-1}).

From the classical electromagnetic theory of oscillating dipoles, Raman peaks have a Lorentzian form:

$$I(\bar{v}) = I_0 \, x \int \frac{d^3\mathbf{k}}{[\bar{\nu} - \bar{\nu}(\mathbf{k})]^2 + \frac{\Gamma_0}{2}} \qquad (Eq. 13)$$

Where Γ_0 is half width and $\bar{\nu}(\mathbf{k})$ is the dispersion branch.

Photon ($\mathbf{k} \sim 0$) scattering via n phonons (wavevectors, $\mathbf{k}_i$) obeys the conservation of momentum:

$$\sum_{i=1}^{i=n} \mathbf{k}_i = \boldsymbol{k}_{scattered} - \boldsymbol{k}_{incident} \qquad (Eq. 14)$$

$$\sum_{i=1}^{i=n} \mathbf{k}_i \sim \mathbf{0} \qquad (Eq.15)^{[40]}$$

Thus, only the vibrations close to the center of Brillioun zone can be active in first order spectrum [41]. On the other hand, not every vibration close to the center of Brillioun zone can be active in first order spectrum. $\left(\frac{\partial a_{ij}}{\partial Q}\right)$ term also must be nonzero to be active in first order spectrum. Hence, it is possible to deduce Raman activity from Group theory.

Raman spectroscopy can be used to gather information about crystallization. Crystallinity of silicon thin films can be found via using the integrated areas:

$$X_c = \frac{I_c + I_i}{\alpha I_a + I_c + I_i} \qquad (Eq.16)$$

Where I_a is the integrated area of amorphous phase, I_i is the integrated area of intermediate phase and I_c is the integrated area of crystalline phase. In Figure 11, an exemplary Raman spectra deconvolution for silicon samples is given. In the semi-quantitative approach, the α factor is rounded to be 1 if the crystalline sizes are quite small [42].

A shift in the 520 cm^{-1} peak can be attributed to the change in the crystalline size and stress within the film. From this information, the average crystalline size can be calculated via using wavenumber shift of TO mode of Si-Si vibration from 520 cm^{-1} using the following empirical formula:

$$d = 2\pi \sqrt{\frac{B}{520 - \bar{\nu}_{peak}}} \qquad (Eq. 17)$$

where $\bar{\nu}_{peak}$ is the peak position, d is the size of crystal and B is a constant value of 2.24 for silicon [43].

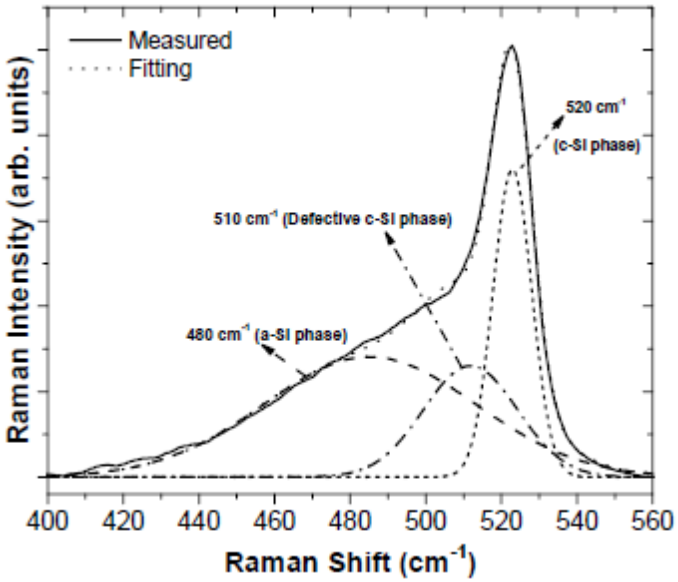

Figure 11: An exemplary Raman spectra deconvolution for silicon sample.

In this thesis study, backscattering Raman measurements were performed with Jobin Yvon Horiba i550 Raman system at room temperature at GÜNAM Measurement Laboratory. Source of excitation was a He-Ne laser with 632.83 nm wavelength. In

order to detect the Raman shifts, we used double mono chromator and Peltier cooled charge-coupled device (CCD) detector with a resolution less than 1 cm^{-1}. Raman spectroscopy measurements were carried out under the same conditions for the accuracy of comparisons.

3.5.2. Fourier Transform Infra-Red (FTIR) Spectroscopy

"Fourier spectroscopy" is used to describe the analysis of any changing signal into its building frequency components. The mathematical methods are named after French mathematician and physicist Jean-Baptiste Joseph Fourier [44] [45] [46]. It is possible to apply Fourier transforms to many different types of spectroscopic techniques such as infrared spectroscopy known as Fourier transform infrared (FT-IR), electron paramagnetic resonance (EPR) and nuclear magnetic resonance (NMR) spectroscopy. FT-IR spectroscopy covers absorption, reflection, emission and photoacoustic spectrum which can be obtained via Fourier transform of an optical interferogram. FT-IR spectroscopy is a very powerful technique due to the fact that it allows simultaneous analysis of many frequency components in one time. Once Fourier technique is applied to different terms of spectroscopy, the technological outcome is a spectrometer that gives the entire spectrum in the amount of time that a classical spectrometer could just scan across a single line in the spectrum. Fourier-based methods are used over a wide spectral range [47] [48] [49]. It is possible to employ FT spectroscopy for a long range of frequencies varying over ultraviolet, visible, near infrared, mid infrared and even far infrared regions via selecting different beam splitters and detectors for the needed ranges. There is not any other dispersive technique which can be used for such a broad range of frequencies.

There are two different kinds of molecular vibrations, which are stretching and bending. There are a total of 3 n degrees of freedom for a molecule having n atoms, where these degrees of freedom corresponds to the Cartesian coordinates of each atom in the molecule. In the case of a nonlinear molecule, three of these degrees are

rotational, three are translational and the remaining are fundamental vibrations. On the other hand, for the case of a linear molecule, two degrees are rotational and three are translational. The net number of fundamental vibrations for nonlinear and linear molecules is given in the table 1.

Table 1: Net number of fundamental vibrations for nonlinear and linear molecules.

Molecule	degrees of freedom
Nonlinear	3n – 6
Linear	3n – 5

IR spectrum is measured via transmitting infrared radiation through the sample and finding the proportion of absorbed incoming radiation at a known frequency. All bonded atoms in a molecule vibrate relative to the each other continuously unless they are at zero degrees Kelvin. When there is a match between the frequency of incident IR radiation and the vibration frequency of molecule, light is absorbed by molecule leading to vibrational motion with that specific frequency. Therefore, the peaks at the absorption spectrum are directly correlated with the molecular vibrations. When molecular vibrations take place, a change in bond length or bond angle occurs.

Change in bond length is called as stretching while bending is the name for the change in bond angle. In Figure 12, vibrational modes of Si-O bonds are given. Depending on the direction of the bending, it can be classified as rocking, wagging, scissoring and twisting. Symmetric stretching occurs once bonds stretch in phase while asymmetric stretching takes place when bonds stretch out-of phase. Since stretching mode does not

lead to a change in electric dipole moment of the symmetric bonds, it does not show any IR absorption peak. Due to the fact that asymmetric vibrations show a larger change in dipole moments, intense IR absorption peaks are observed for asymmetric vibrations.

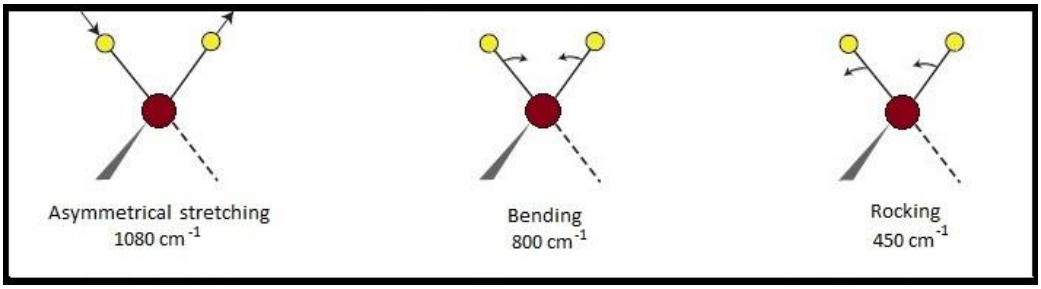

Figure 12: Vibrational modes for Si-O bonds.

Infrared is referring to the part of the electromagnetic spectrum between the visible and microwave regions. The IR region is constituted of three regions: the near, mid, and far IR. In this thesis study, we prefer to give the results in wavenumbers (cm^{-1}); however, another unit, wavelength (μm) can also be used.

The conversion between wavenumbers and wavelength can be carried out via the following equation:

$$\bar{\nu}\ (cm^{-1}) = \frac{10^4}{\lambda\ (\mu m)} \qquad (Eq.18)$$

Mid-IR region is in between 400 - 4000 cm^{-1} in wavenumbers. There are four different regions in this spectrum. First part lies in the 4000 - 2500 cm^{-1} region and it is related with the hydrogen (O-H, C-H, N-H, etc.) stretching mode. Second part lies in the 2500 – 2000 cm^{-1} region, and it is related with the triple bond stretching absorption because of the high force constant between bonds. Third part lies in the 2000 to 1500 cm^{-1} region, which is related with the double bond vibrations. Last region is in between 1500-600cm^{-1}. This range is the most significant part because sample detection from the wavenumber positions of the absorption band is carried out usually in this region. In table 2, vibration modes and the corresponding wavenumbers are given for Si-O bonds.

Table 2: Vibration modes and corresponding wavenumbers for Si-O bonds.

Vibration mode	Wavenumber (cm^{-1})
Rocking	450
Bending	800
out of plane deformation	1080

In this thesis study, FTIR measurements were carried out with a Bruker Ekinox 55 spectrometer to monitor the vibrational modes for Si-O bonds at a normal incidence The resolution of measurements was 2 cm^{-1} between the wave numbers 400 and 4000 cm^{-1}. To get the background signal, an unprocessed Si substrate from the same wafer batch was used, that was then subtracted from the FTIR data of the processed sample

to eliminate the phonon modes of the Si substrate. FTIR Measurements were carried out under the same conditions for the accuracy of comparisons.

2.5.3. X-Ray Photoelectron Spectroscopy (XPS)

X-ray Photoelectron Spectroscopy (XPS), also known as Electron Spectroscopy for Chemical Analysis (ESCA), is a spectroscopic technique which is used for analyzing the surface chemistry of a material. Via use of XPS various information can be gathered such as elemental composition, empirical formula, chemical state and electronic state of the elements within a material.

Although the history of X-ray photoelectron spectroscopy can be dated back to the Einstein's explanation of the photoelectric effect [50], the photoelectric effect has been utilized for studying the composition and electronic structure of matter by Kai Siegbahn, who received the Nobel Prize in 1981 for his tremendous discovery [51].

The sample to be analyzed is placed in an ultrahigh vacuum conditions, then monochromatic x-ray source sends soft (low energy) X-ray to the sample surface. X-ray leads to the excitation atoms. For the case, when the binding energy of the electrons of the sample is lower than the X-ray energy, X-ray leads to the excitation atoms. Electrons are emitted from initial state with a kinetic energy, E_k, depending on the energy of incident X-ray and binding energy of the atomic orbital. While being exposed to soft X-ray, kinetic energies of the emitted electrons are also measured. Binding energy of the atomic orbital is characteristic for each element. Therefore, the source of information in XPS is the energy analysis of emitted electrons.

Because of the fact that the energy of an X-ray with particular wavelength is known and since the kinetic energies of emitted electrons are measured, the binding energy of the atomic orbital of each of the emitted electrons can be found via using the following equation:

$$E_{binding} = E_{photon} - (E_{kinetic} + \phi) \qquad (Eq. 19)$$

Where $E_{binding}$ the binding energy of the electron is, E_{photon} is the energy of the incoming X-ray photons, $E_{kinetic}$ is the kinetic energy of the electron measured via the instrument and ϕ is the work function depending on both the spectrometer and the material. This equation is essentially nothing but the conservation of energy equation. The work function ϕ can be arranged accordingly via instrumental correction factor which replaces the few eV of kinetic lost by the photoelectron once absorbed by the detector.

In this thesis study, X-ray Photoelectron Spectroscopy (XPS) was used to gather information on composition and chemical bonding state of the films using a Specs Ea 300 system. The X-ray source was a monochromatized Al Kα line.

CHAPTER 4

RESULTS AND DISCUSSION

4.1. Properties of As Deposited Samples

Figures 13 and 14 show the Raman spectra of samples deposited at room temperature (RT) and samples deposited at high temperature (HT, 400^0 C) on silicon wafer substrate and quartz substrate respectively. The Raman spectra of silicon wafer and quartz were also shown for comparison. In the Raman spectra of samples deposited on Si wafer substrate, the peak positioned at 520 cm^{-1} being interpreted as coming from the vibration mode of crystalline Si. From the comparison with the as-deposited films on the quartz substrate, we could come to the conclusion that the source of these crystalline Si signals is the silicon substrate since there is no such a signal in the Raman spectra of the as-deposited films on the quartz substrate.

The as deposited films both on the quartz and silicon substrates show a broad signal between 350 to 630 cm^{-1}. This broad signal was previously attributed to SiO [52]. In this broad signal, there are two distinct broad peaks. First is at around 435 cm^{-1} and the second is at around 560 cm^{-1}. Despite the fact that the intensity of the first peak is greater than the second for the samples deposited on quartz substrate, it is vice versa for the samples deposited on silicon wafer substrate. This change is attributed to the intensity contribution of background signal arising because of the ω_1 network mode of quartz substrate at 440 cm^{-1}. This explanation is in a well agreement with the fact that as deposited samples on quartz substrate exhibit a background signal arising due to the transverse optical – longitudinal optical pair at around 800 cm^{-1} while there is no such a peak present for as deposited samples on silicon wafer substrate.

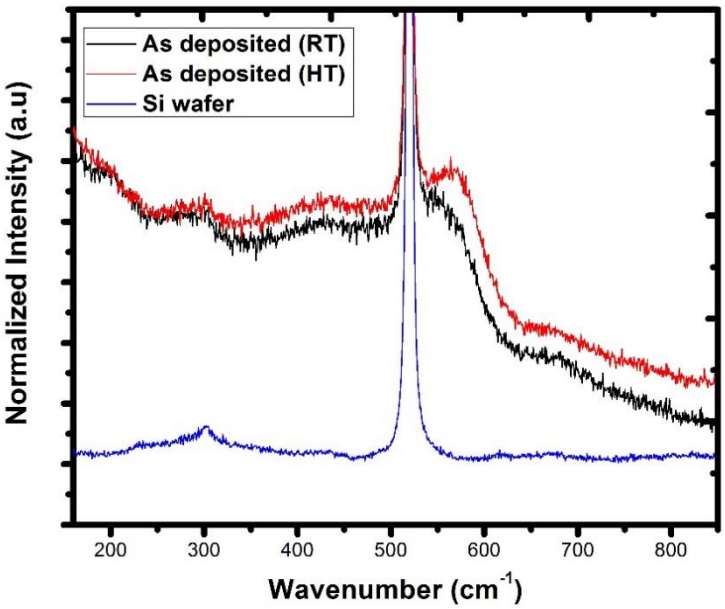

Figure 13: Raman spectra of Si wafer and samples deposited on Si wafer substrate at RT and HT.

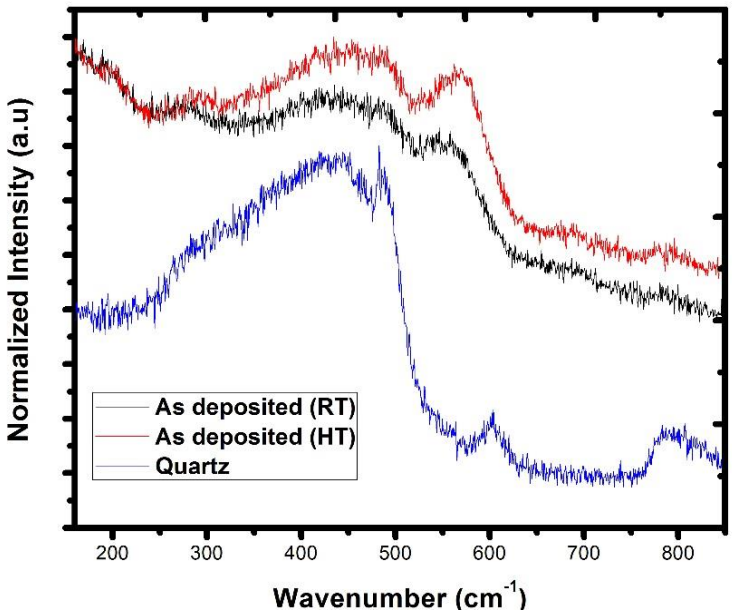

Figure 14: Raman spectra of bare quartz and samples deposited on quartz substrate at RT and HT.

When the RT as deposited and HT as deposited samples are compared, both of the RT as deposited and HT as deposited samples show the broad signal between 350 to 630 cm^{-1} and also the first and second peaks at around 435 and 560 cm^{-1} respectively. This fact is valid for samples both on the quartz and silicon wafer substrates. Because of the fact that there is no different peak observed for RT as deposited and HT as deposited samples, the composition of films stays the same at deposition temperatures of RT and HT.

It is seen that the first and second peak intensities are greater for HT as deposited samples both on the quartz and silicon wafer substrates. This increase in peak intensity might be due to the difference between the amount of Si monoxide clusters $(SiO)_n$ for RT as deposited and HT as deposited samples. Surface mobility, re-evaporation and cluster formation of surface molecules on the substrate are heavily affected via substrate temperature. It is expected that the room temperature deposited molecules on the substrate lose their kinetic energy in a very short time and settle on their position on the substrate surface. Because of the fact that mobility of the room temperature deposited molecules are quite low, the deposited molecules tend to condense as thin amorphous films. As the substrate temperature increases, the kinetic energy of the deposited molecules also increase. This leads to an enhancement in the probability of overcoming the surface barrier for added molecules, which would foster the formation of more Si monoxide clusters $(SiO)_n$ via movement of added molecules to deeper levels. Molecules having weak adhesive strength are expected to leave the substrate surface due to re-evaporation, which can also help the genesis of Si monoxide clusters $(SiO)_n$. The provided energy difference between the HT as deposited and the RT as deposited samples can be enough for the for the formation of more Si monoxide clusters $(SiO)_n$, while this energy difference is not enough for the genesis of more separate Si since most of the Si-Si bonds are expected to be formed after the formation of Si monoxide clusters $(SiO)_n$. After the formation of Si monoxide clusters $(SiO)_n$, once enough amount of energy provided, clusters can come together and make bond with other clusters and prefer to form Si-Si bonds based on the analysis of their frontier

orbitals via Becke-type three-parameter density functional theory calculations [53] or sp^3 Si cores can be formed inside Si oxide clusters and such clusters are expected to lead to nucleation of Si through the combination of small Si suboxide clusters based on the work where the generalized gradient approximation corrections in the form of Perdew, Burke, and Ernzerhof and the double plus polarization orbital basis sets were employed for density functional theory calculations [54].

XPS and FTIR analyses of samples were performed to further confirm the abovementioned argument that the difference in peak intensities might arise because of the difference between the amount of Si monoxide clusters $(SiO)_n$ for RT as deposited and HT as deposited samples while there is no chemical difference among them.

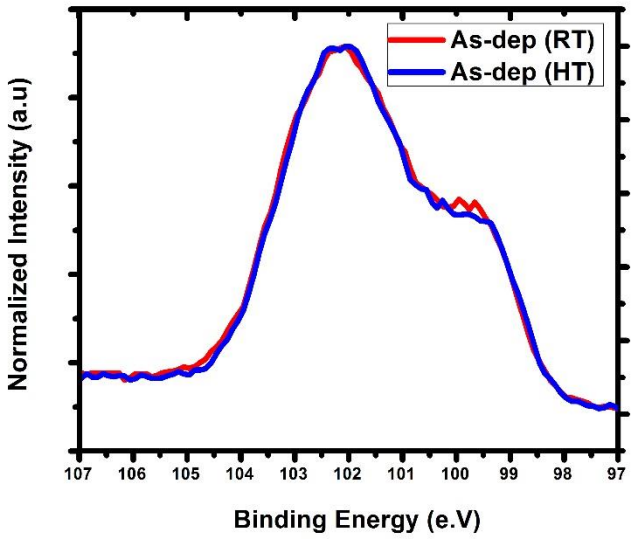

Figure 15: XPS spectra of RT deposited and HT deposited samples on the Si wafer substrate.

In Raman spectroscopy analysis, the effect of deposition temperature on as deposited samples was analyzed and some structural differences was observed although no information was obtained referring to any differences in the chemistry of HT as deposited and RT as deposited samples. The effect of the deposition temperature on the chemistry of the as deposited samples was revealed via XPS. In Figure 15, XPS spectra of RT as deposited sample on the silicon wafer substrate and HT as deposited sample on silicon wafer substrate are given. No distinctive difference between the RT as deposited and HT as deposited samples was observed. To also understand the effect of substrate on the chemistry of films, XPS was employed. In Figure 16, XPS spectra of HT as deposited samples on the quartz substrate and Si wafer substrate are given. XPS spectra results show that the chemical structure of samples was not affected via the substrate type.

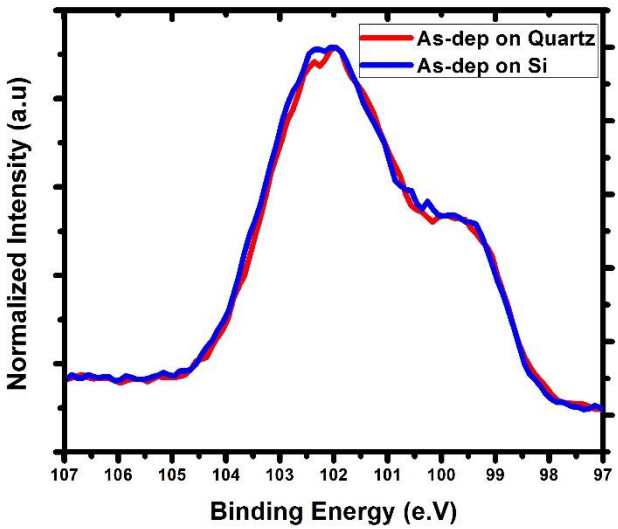

Figure 16: XPS spectra of HT as deposited sample on the silicon wafer substrate and HT as deposited sample on the quartz substrate.

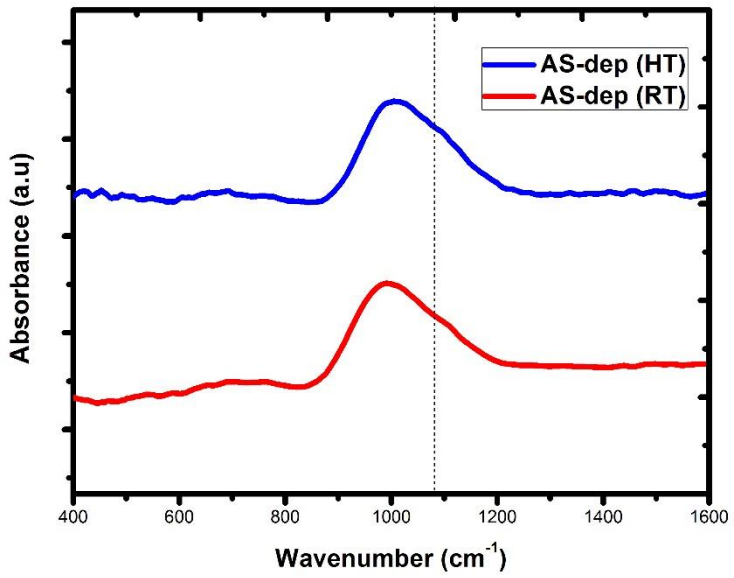

Figure 17: FTIR spectra of RT as deposited and HT as deposited samples on Si wafer substrate.

In order to gather information on chemical structure of the HT as deposited and RT as deposited samples, FTIR was also employed. In Figure 17, FTIR spectra of HT as deposited and RT as deposited samples on Si wafer substrate are given. In spite of the fact that the peak position corresponding to asymmetric stretching mode of SiO_2 is at around 1081 cm^{-1}, peak intensity, peak position and shape of the absorption band is heavily affected by the film stoichiometry. The peak position corresponding to asymmetric stretching mode of SiO_2 is also shown for comparison. Once the x value in SiO_x decreases to lower values, it is expected that the peak position shifts to lower wavenumbers [55] [56] [57]. When RT as deposited sample and HT as deposited samples are compared, both of the peak positions are quite distant from the 1081 cm^{-1} since the value of x in SiO_x is smaller than 2. In addition to this, the peak related to the rocking mode generally observed at around 450 cm^{-1} is not present for both of the HT as deposited and RT as deposited samples. Moreover, the peak related to the bending

mode giving rise at around 800 cm^{-1} is also not present for both of the HT as deposited and RT as deposited samples. Therefore, no obvious difference between RT as deposited sample and HT as deposited sample was observed.

4.2. Effect of Annealing Temperature for One hour Annealed Samples

In the Figure 18, Raman spectra of samples deposited on silicon wafer substrate, and subsequently annealed at temperatures 800^0 C and 900^0 C for one hour are given. The Raman spectra of silicon wafer and amorphous silicon were also shown for comparison. For both samples, the peak positioned at 520 cm^{-1} is interpreted as coming from the vibration mode of crystalline Si. From the comparison with the samples on quartz substrate after annealing at temperatures 800^0 C and 900^0 C for one hour, which is shown in Figure 19, it can be deduced that the source of these crystalline Si signals is the silicon substrate since there is no such a signal in the Raman spectrum of the films on the quartz substrate.

Raman spectra of samples on silicon wafer substrate exhibits amorphous Si peaks at around 160 and 480 cm^{-1}, that can be clearly seen at annealing temperatures 800^0 C and 900^0 C. Although the smooth tail between 250 and 350 cm^{-1} in the Raman spectrum of amorphous Si was also observed at annealing temperature 900^0 C, there is a sharper transition to lower wavenumbers at annealing temperature 800^0 C. This difference between annealing temperatures 800^0 C and 900^0 C is also seen for the samples deposited on quartz substrate (Fig. 19). This difference might be due to several reasons. First reason can be the increase in the amount of amorphous Si and the second can be the coarsening of amorphous Si nanoclusters. The obvious existence of amorphous phase on the Raman spectrum even at high temperatures are because of the phase separation of the silicon suboxides (Si_2O, SiO and Si_2O_3) and the formation of new amorphous Si nanoclusters. Therefore, phase separation of Si takes place before the crystallization starts.

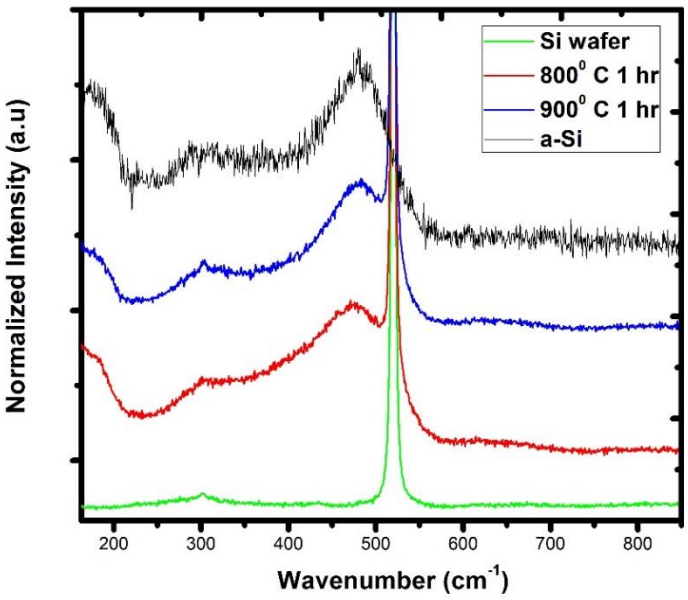

Figure 18: Raman spectra of amorphous Si, Si wafer and samples deposited on silicon wafer substrate, and subsequently annealed at temperatures 800^0 C and 900^0 C for one hour.

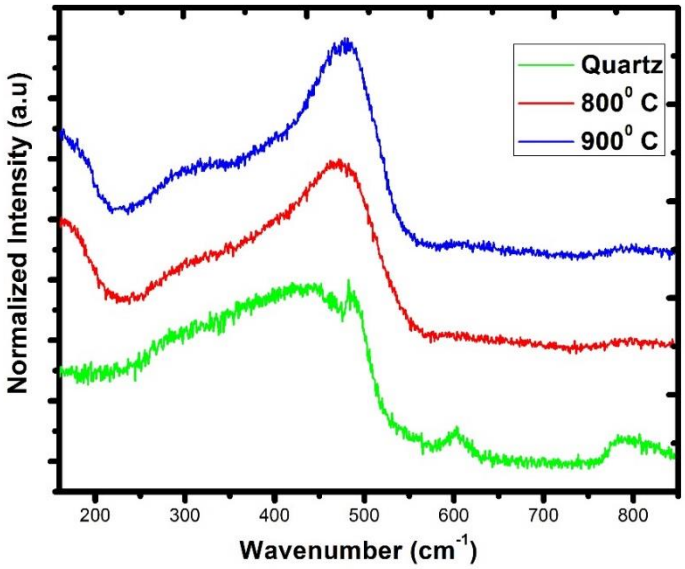

Figure 19: Raman spectra of quartz and samples deposited on quartz substrate, and subsequently annealed at temperatures 800^0 C and 900^0 C for one hour.

In Figure 20, FTIR spectra of samples deposited on Si wafer substrate, and subsequently annealed at temperatures 800^0 C and 900^0 C for one hour are given. For comparison, the peak position corresponding to the native oxide is shown with dashed lines. This peak position also signifies the formation of SiO_2. After annealing at a temperature of 800^0 C for one hour, the peak position corresponding to asymmetric stretching mode shifts to 1069 cm^{-1} and a shoulder appears at the right side. The appearance of this shoulder is attributed to the TO_2 mode, also known as surface mode. In addition to this, two peaks were observed, which were not present in the FTIR spectrum of the as deposited sample. First, the peak corresponding to the rocking mode was observed at around 450 cm^{-1}. Second, the peak related to the bending mode giving rise at around 800 cm^{-1} was present.

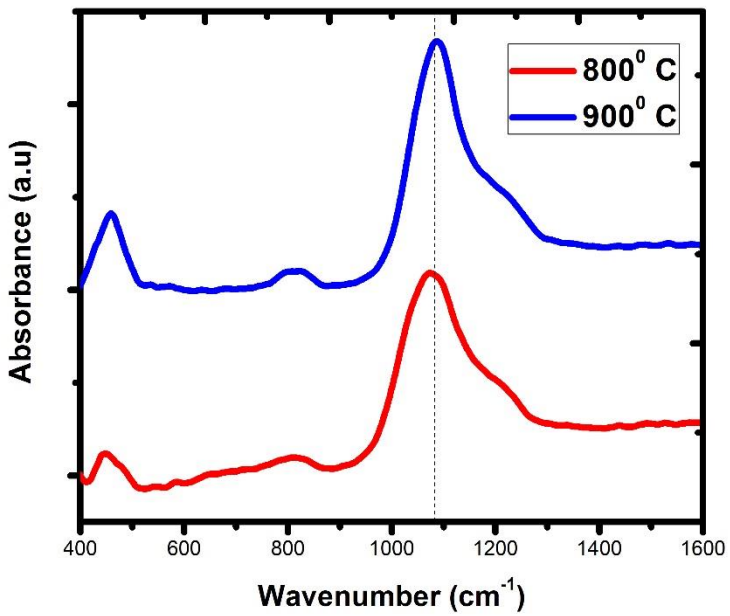

Figure 20: FTIR spectra of samples deposited on silicon wafer substrate, and subsequently annealed at temperatures 800^0 C and 900^0 C for one hour.

After annealing at a temperature of 900^0 C for one hour, the peak position related to asymmetric stretching mode shifted to higher values indicating that SiO_2 is formed due to the phase separation of suboxides. This further confirms the phase separation difference between 800^0 and 900^0 C annealed samples. The intensity of the peak corresponding to the rocking mode increased and the peak related to the bending mode became more obvious. Similar to the sample annealed at 800^0 C, this sample also exhibits a shoulder at the right side of the main peak. This shoulder is also due to the TO_2 mode.

Figures 21 shows the Raman spectra of samples deposited on silicon wafer substrate, and subsequently annealed at temperatures 1000^0 C, 1100^0 C and 1200^0 C for one hour. Although an obvious amorphous Si peak at 480 cm^{-1} was present for annealing temperatures 800^0 C and 900^0 C, it was not observed in the Raman spectrum of the sample annealed at 1000^0 C. On the other hand, the crystal Si peak positioned at 520 cm^{-1} is strongly asymmetric. This crystal Si peak asymmetry phenomena was observed in some studies on Si nanocrystals [58] [59]. Amorphous Si peak at 480 cm^{-1} may not be observed once the concentration of amorphous Si is low; however, it can cause a strong asymmetry in the crystal Si peak positioned at 520 cm^{-1}. Therefore, increasing the annealing temperature to 1000^0 C leads to crystallization of most of the amorphous Si while a small portion of it still exists. The broad peak at around 160 cm^{-1} further confirms the existence of amorphous Si. Since the amount of amorphous Si is quite low, the intensity of this peak is also quite low. When the annealing temperature is increased to 1100^0 C, the asymmetry of crystal Si peak decreased indicating the crystallization of more amorphous Si. Finally, once the annealing temperature reached 1200^0 C, asymmetry of the crystal Si peak disappeared and it became completely symmetric showing the complete crystallization of film.

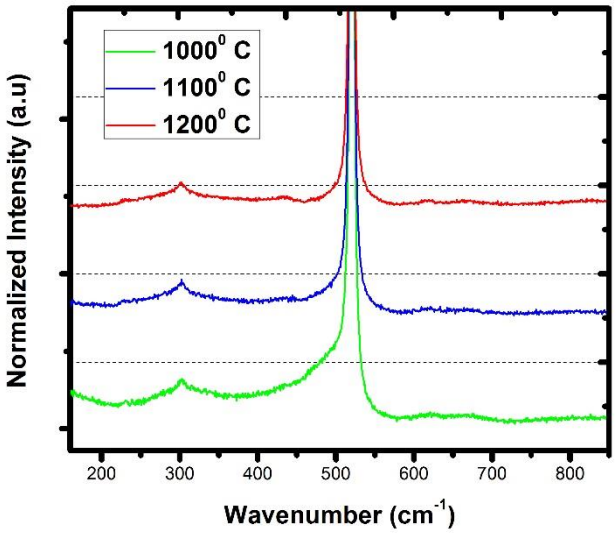

Figure 21: Raman spectra of samples deposited on silicon wafer substrate, and subsequently annealed at temperatures 1000^0 C, 1100^0 C and 1200^0 C for one hour.

Raman spectra and normalized Raman spectra of samples deposited on quartz substrate, and subsequently annealed at temperatures 1000^0 C, 1100^0 C and 1200^0 C for one hour are given in Figures 22 and 23, respectively. In the Raman spectra of all of these samples, several peaks were observed that were not present for the samples deposited on silicon wafer substrate. This different peaks are interpreted as the intensity contribution of quartz substrate background. The signal at around 491 cm^{-1} appears due to the vibrational mode of SiO_4 tetrahedra with a non-bridging oxygen atom. This explanation is also confirmed via the fact that the these samples on quartz substrate also exhibits a background signal at 607 cm^{-1} arising due to the β-cristobalite structure generating a $(SiO)_3$ ring D_2 band. Lastly, the transverse optical – longitudinal optical pair gives a peak at around 800 cm^{-1}.

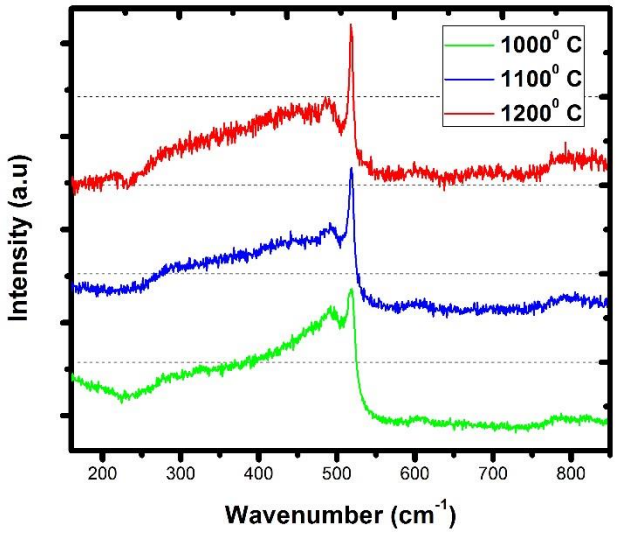

Figure 22: Raman spectra of samples deposited on quartz substrate, and subsequently annealed at temperatures 1000^0 C, 1100^0 C and 1200^0 C for one hour.

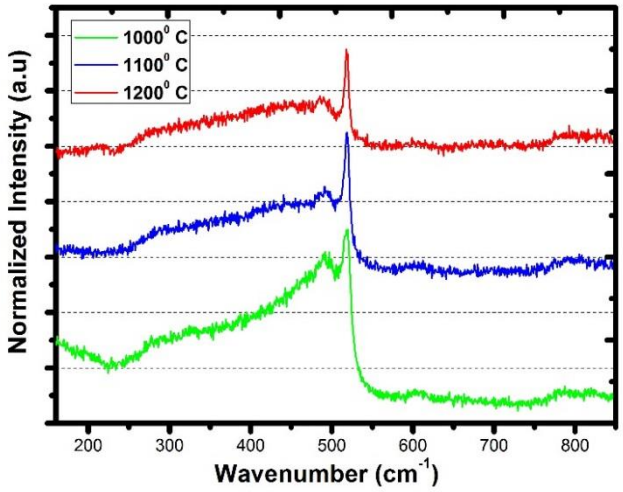

Figure 23: Normalized Raman spectra of samples deposited on quartz substrate, and subsequently annealed at temperatures 1000^0 C, 1100^0 C and 1200^0 C for one hour.

The Raman spectrum of 1000^0 C annealed sample on quartz substrate also exhibits a broad peak with a low intensity at around 160 $cm^{-1,}$ which also supports the existence of small amount of amorphous Si. Once the annealing temperature reached 1100^0 C, the crystal Si peak asymmetry obviously decreased showing the crystallization of more amorphous Si. When the annealing temperature increased to 1200^0 C, asymmetry of the crystal Si peak further decreased. However, it is not completely symmetric while the crystallization is completed as we know from the information that the films on silicon wafer substrate provided. The reason of asymmetry is attributed to the background signal arising due to the quartz substrate.

FTIR spectra of samples deposited on silicon wafer substrate, and subsequently annealed at temperatures 1000, 1100 and 1200^0 C for one hour are given in the Figure 24. For comparison, the peak position of corresponding to the native oxide is shown with dashed lines. This peak position also shows the formation of SiO_2. At all these annealing temperatures, the peak corresponding to the rocking mode was observed at around 450 cm^{-1}, the peak related to the bending mode giving rise at around 800 cm^{-1} was present. From the comparison of asymmetric stretching mode peak positions of samples with the dashed line, it can be concluded that SiO_2 is formed due to the phase separation of suboxides.

In the FTIR spectra of all these samples, a shoulder appeared at the right side of the main peak. For the samples annealed at 1100^0 C and 1200^0 C, another peak was observed at around 1130 cm^{-1}, which arise because of the surface mode.

The effect of the annealing temperature on the chemical structure of samples was also revealed via XPS. In Figure 25, XPS spectra of as deposited sample on silicon wafer substrate and samples deposited on silicon wafer substrate, and subsequently annealed at temperatures 800 and 1100^0 C for one hour are given.

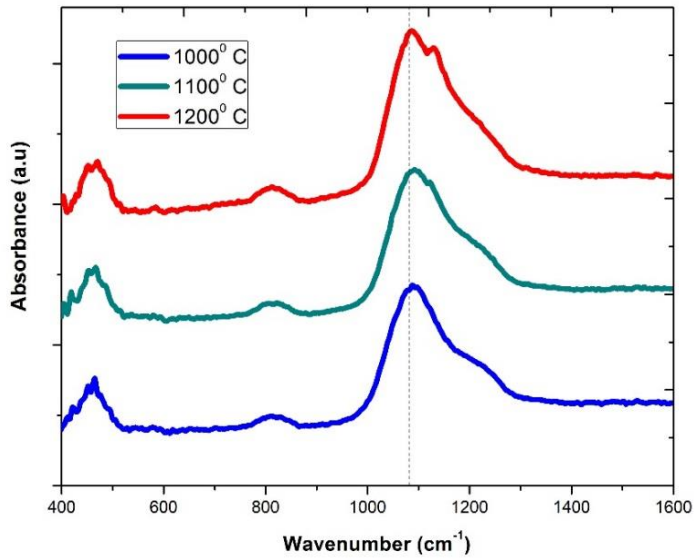

Figure 24: FTIR spectra of samples deposited on silicon wafer substrate, and subsequently annealed at temperatures 1000, 1100 and 1200^0 C for one hour.

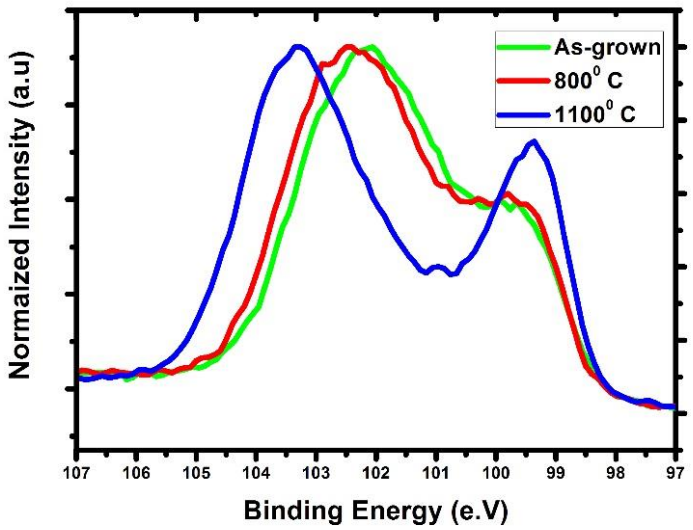

Figure 25: XPS spectra of as deposited sample on silicon wafer substrate and samples deposited on silicon wafer substrate, and subsequently annealed at temperatures 800 and 1100^0 C for one hour.

As the annealing temperature is increased, suboxides were eliminated via phase separation to two poles where elemental Si and SiO_2 dominates the environment. When compared to the as-deposited sample, a small increase in elemental Si can be observed in the sample annealed at 800^o C, which is expected to come from amorphous Si, as discussed earlier (Figs. 18 and 19). The XPS spectrum for the sample annealed at 1100^o C strongly suggests an increase in elemental Si as well as Si^{+4} at the expense of partial oxidic states, which verifies the disproportionation reaction.

4.3. Effect of Annealing Time for Samples Annealed at 800^0 C

In this thesis study, the minimum annealing temperature was 800^0 C. For one hour of annealing, no crystallization was observed despite the fact that phase separation of amorphous Si was obvious in the Raman spectra. It is important to see the effect of annealing at 800^0 C for higher amount of annealing times to understand whether crystallization can start at 800^0 C or there is a temperature threshold for the start of crystallization that would not allow crystallization at 800^0 C. Raman spectra of samples deposited on quartz substrate, and subsequently annealed at 800^0 C for 1 hour, 20 hours and 68 hours are given in the Figure 26. From the Raman spectra, it is obvious that there is no crystallization even for 68 hours of annealing at 800^0 C. As a result of this fact, it appears that there is a minimum temperature limit for the start of crystallization in such a Si-O system. Raman spectra of these samples on quartz substrate exhibits amorphous Si peaks at around 160 and 480 cm^{-1}, that was also present in the Raman spectrum of 1 hour annealed sample at 900^0 C. Despite the fact that the smooth tale between 250 and 350 cm^{-1} in the Raman spectrum of amorphous Si was also seen at annealing times 20 and 68 hours, there is a sharper transition to lower wavenumbers for 1 hour annealing. This difference between annealing times 1 hour and extended annealing times is also seen for the samples deposited on silicon wafer substrate given in Figure 27. The reason of this difference may lie under several reasons. Firstly, provided extra energy can induce more phase separation of the silicon suboxides (Si_2O, SiO and Si_2O_3). This extra energy can also lead to the formation of new amorphous Si nanoclusters.

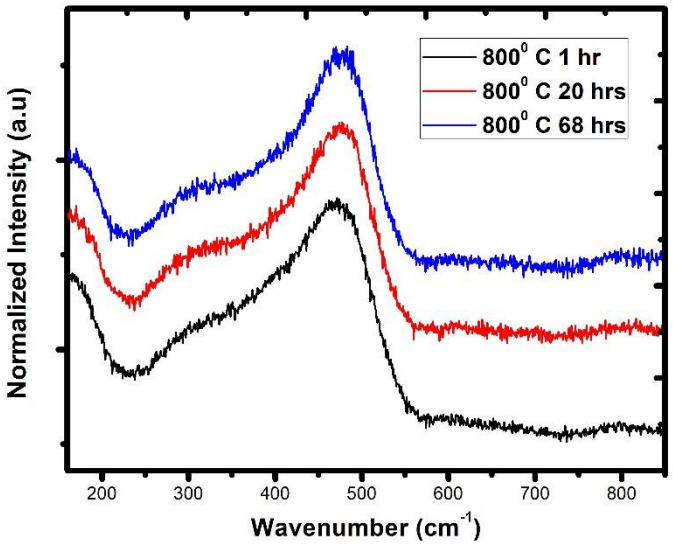

Figure 26: Raman spectra of samples deposited on quartz substrate, and subsequently annealed at 800^0 C for 1 hour, 20 hours and 68 hours.

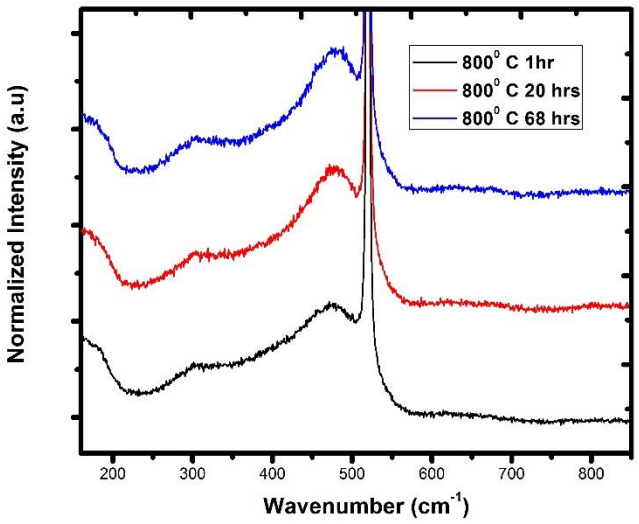

Figure 27: Raman spectra of samples deposited on silicon wafer substrate, and subsequently annealed at 800^0 C for 1 hour, 20 hours and 68 hours.

The Raman spectroscopy results revealed that phase separation and formation of detectable amount of amorphous Si was observed for sample annealed at 800^0 C for one hour and the amount of Si increased when the annealing time was increased to 68 hours. In Figure 28, XPS spectra of samples deposited on silicon wafer substrate, and subsequently annealed at 800^0 C for 1 hour and 68 hours are given. XPS spectra results are in a well agreement with the Raman spectroscopy results that the amount of Si increases, phase separation to Si and SiO_2 poles takes place as the annealing time is increased to 68 hours from 1 hour.

In Figure 29, FTIR spectra of samples deposited on silicon wafer substrate, and subsequently annealed at 800^0 C for 1 hour, 20 hours and 68 hours are given. For the purpose of comparison, the peak position corresponding to the native oxide is shown with dashed lines. Despite the fact that the peak position corresponding to asymmetric stretching mode is positioned at 1069 cm^{-1} for 1 hour annealed sample, this peak shifted to higher values for 20 hours and 68 hours of annealing, indicating SiO_2 formation. This is in a well agreement with the results obtained from Raman spectroscopy and XPS that there is an increase in the amount of Si because of the fact that phase separation to Si and SiO_2 poles takes place as the annealing time is increased to 68 hours from 1 hour.

In the FTIR spectra of all these samples a shoulder appears at the right side of AS mode peak. The appearance of this shoulder is because of the TO_2 mode. Moreover, FTIR spectra of samples exhibited two more peaks. First, the peak related to the rocking mode was observed at around 450 cm^{-1}. Second, the peak corresponding to the bending mode giving rise at around 800 cm^{-1} was present.

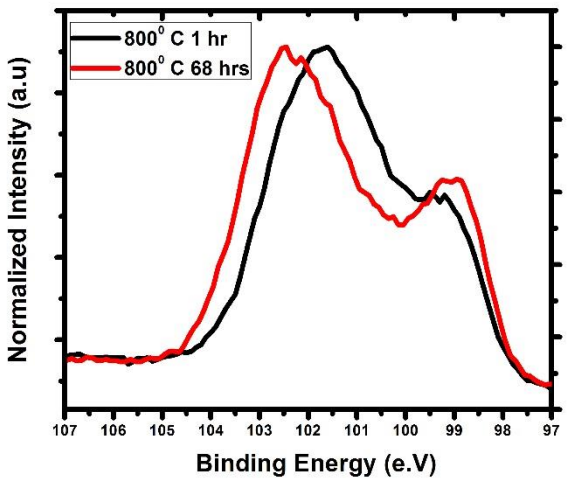

Figure 28: XPS spectra of samples deposited on silicon wafer substrate, and subsequently annealed at 800^0 C for 1 hour and 68 hours.

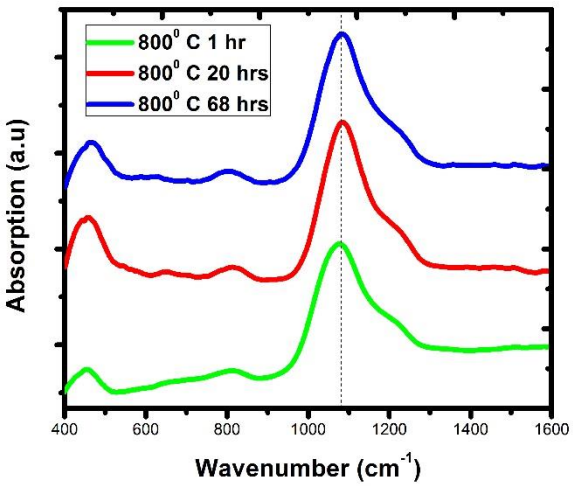

Figure 29: FTIR spectra of samples deposited on silicon wafer substrate, and subsequently annealed at 800^0 C for 1 hour, 20 hours and 68 hours.

4.4. Effect of Annealing Time for Samples Annealed at 900^0 C

Due to the fact that no crystallization was observed at 800^0 C even for extended amount of annealing times, a question arises that: can crystallization take place for extended amount of annealing times at 900^0 C. Then annealing studies at 900^0 C for extended amount of times were carried out to so as reveal the impact of annealing time at this temperature to understand the mechanism. Raman spectra of samples deposited on quartz substrate, and subsequently annealed at 900^0 C for 1 hour, 3 hours, 6 hours, 20 hours and 68 hours are given in the Figure 30. Raman spectra of 1 hour, 3 hours and 6 hours annealed samples exhibit amorphous Si peak at around 160 cm^{-1}. There is no crystal Si peak located at 520 cm^{-1} for 1 hour annealed sample. For 3 hours annealed sample, there is also no crystal Si peak located at 520 cm^{-1}. However, at around 520 cm^{-1}, a shoulder is present that we did not observe for 1 hour annealed sample. Therefore, the crystallization starts between the first hour and third hours in the annealing process. When the annealing time reached 20 hours, a radical decrease in the intensity of amorphous Si peak, located at around 160 cm^{-1}, was observed. The amount of amorphous Si decreased as the annealing temperature was increased to 20 hours from 6 hours due to crystallization; as a result, the amorphous Si peak at around 160 cm^{-1} disappeared. However, at 20 hours of annealing, the Raman spectrum did not become completely flat due to the remaining amorphous Si. Even for 68 hours of annealing at 900^0 C, that small amorphous Si peak did not disappear in spite of the fact that the intensity of crystal Si peak increased. This is because of the fact that phase separation of the silicon suboxides (Si_2O, SiO and Si_2O_3) led to the formation of some new amorphous Si, while already existing amorphous Si was crystallizing. This shows that phase separation and crystallization are two separate processes even at relatively high temperatures.

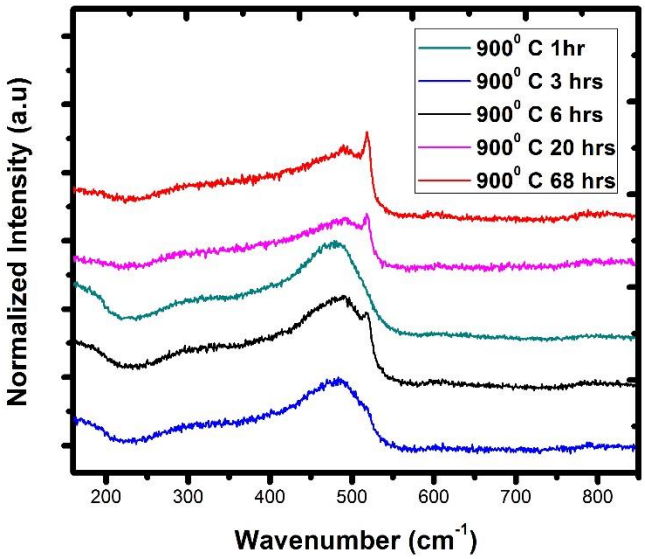

Figure 30: Raman spectra of samples deposited on quartz substrate, and subsequently annealed at 900^0 C for 1 hour, 3 hours, 6 hours, 20 hours and 68 hours.

4.5. Effect of Annealing Time for Samples Annealed at 1100^0 C

In one hour of annealing set of study, it was observed that the crystallization is completed at 1200^0 C. Then annealing studies at 1100^0 C for shorter and extended amount of times were carried out to reveal the effect of annealing time at this temperature so as to understand the mechanism.

Raman spectra of samples deposited on Si wafer substrate, and subsequently annealed at 1100^0 C for 30 minutes, 1 hour, 3 hours and 20 hours are given in the Figure 31. In the Raman spectrum of the sample annealed at 1100^0 C for 30 minutes, there is no obvious amorphous Si peak at 480 cm^{-1}. However, the crystal Si peak located at 520 cm^{-1} is strongly asymmetric. As previously discussed, amorphous Si peak at 480 cm^{-1} may not be seen when the concentration of amorphous Si is low. On the other hand, this low concentration of amorphous Si can induce a strong asymmetry in the crystal Si peak positioned at 520 cm^{-1}. As a result, annealing temperature of 1100^0 C for 30

minutes led to crystallization of most of the amorphous Si while a small portion of it still remains. When the annealing time was increased to 1 hour at 1100^0 C, the asymmetry of crystal Si peak decreased indicating the crystallization of more amorphous Si. Then, as the annealing time was increased to 3 hours at 1100^0 C, the asymmetry of crystal Si peak further decreased with more crystallization of more amorphous Si. Finally, when the annealing time reached 20 hours, asymmetry of the crystal Si peak decreased a lot more than the ones before. On the other hand, even for 20 hours of annealing, the asymmetry in the crystal Si peak did not disappear indicating that there is still some amorphous Si in the system. A fully symmetric Raman spectrum of a sample on Si wafer substrate was previously shown for the case of annealing temperature 1200^0 C.

The annealing studies at 1100^0 C for shorter and extended amount of times were also carried out for samples deposited on quartz substrate to obtain complementary information in order to reveal the effect of annealing time at this temperature so as to understand the mechanism. Raman spectra of samples deposited on quartz substrate, and subsequently annealed at 1100^0 C for 30 minutes, 1 hour, 12 hours and 20 hours are given in the Figure 32. Once the annealing time is increased, the crystal Si peak asymmetry obviously decreases also for the samples on quartz substrate showing the crystallization of more amorphous Si. When the annealing time is increased to 20 hours, asymmetry of the crystal Si peak further decreases. On the other hand, it is not fully symmetric. The reason of asymmetry is attributed to remaining amorphous Si and the background signal arising due to the quartz substrate.

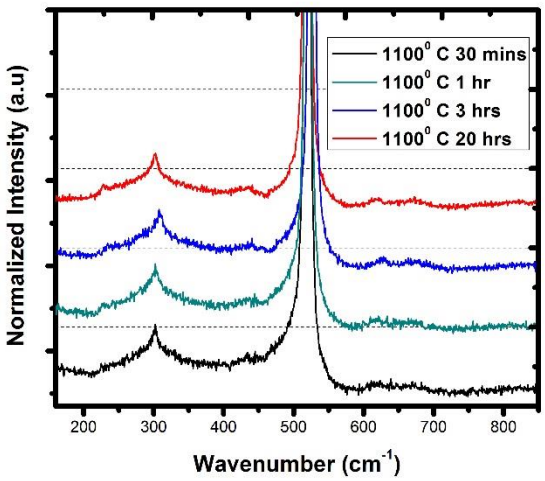

Figure 31: Raman spectra of samples deposited on Si wafer substrate, and subsequently annealed at 1100^0 C for 30 minutes, 1 hour, 3 hours and 20 hours.

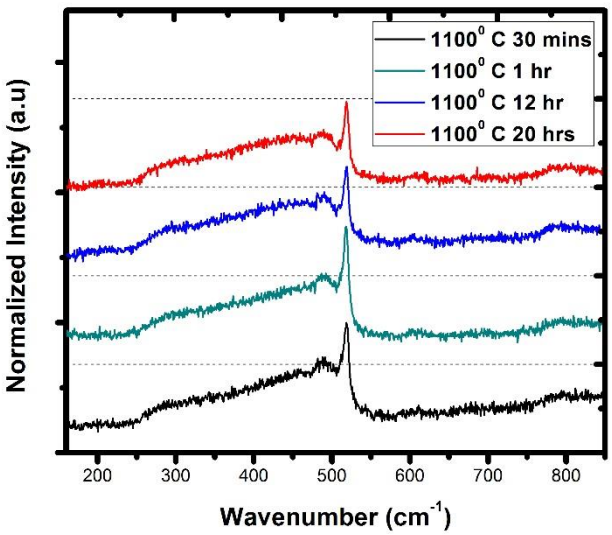

Figure 32: Raman spectra of samples deposited on quartz substrate, and subsequently annealed at 1100^0 C for 30 minutes, 1 hour, 12 hours and 20 hours.

4.6. Effect of Deposition Temperature on Post-Annealing

The effect of deposition temperature on the structure, chemistry and phase separation of as deposited films was previously discussed in chapter 4.1. It was observed that the provided energy difference between the sample deposited at high temperature (HT, 400^0 C) and sample deposited at room temperature (RT) may be enough for the formation of more Si monoxide clusters $(SiO)_n$, while this energy difference is not enough for the genesis of more separate Si because most of the Si-Si bonds are expected to be formed after the formation of Si monoxide clusters $(SiO)_n$. Therefore, it was expected that once enough amount of energy provided via post annealing, an enhanced phase separation should be observed for HT deposited films since the difference between the amount of Si monoxide clusters $(SiO)_n$ can set a base for the genesis of more elemental Si, where Si-Si bonds are expected to be formed after the formation of Si monoxide clusters $(SiO)_n$ via cluster to cluster bonding discussed in chapter 4.1 in details.

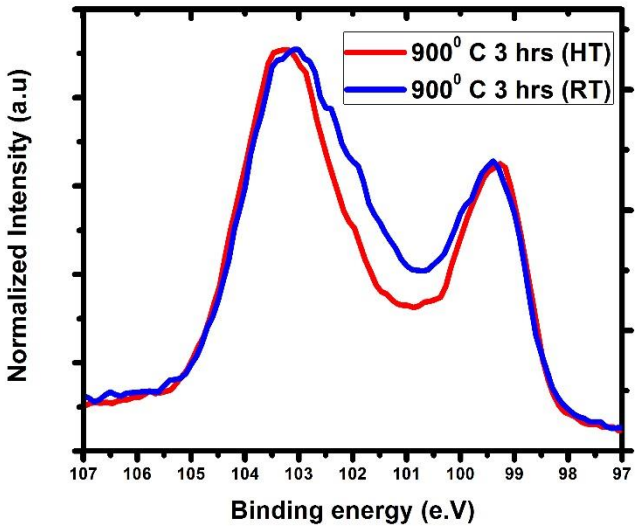

Figure 33: XPS spectra of samples deposited on quartz substrate at RT and HT, and subsequently annealed at 900^0 C for 3 hours.

In Figure 33, XPS spectra of samples deposited on quartz substrate at RT and HT, and subsequently annealed at 900^0 C for 3 hours are given. A clear phase separation difference between the RT deposited and HT deposited samples was observed. After post-annealing, HT deposited sample more rapidly phase separated than RT deposited sample as expected due the difference between the amount of Si monoxide clusters $(SiO)_n$ at the beginning of annealing.

CHAPTER 5

CONCLUSION

In this thesis study, silicon oxide thin films were synthesized via e-beam evaporation of SiO. A broad range of annealing times and temperatures were spanned to reveal crystallization and phase separation mechanism of thin films deposited via SiO target. Effect of deposition temperature on the structure and chemistry of films were investigated. Moreover, the effect of deposition temperature on the post-annealing process was studied. Thin films were characterized with different diagnostics equipment. Raman spectroscopy, X-ray photoelectron spectroscopy (XPS) and Fourier Transform Infrared Spectroscopy (FTIR) were employed to study the mechanism of crystallization and phase separation of films.

This study investigated whether a commercially available solid SiO can be considered as a mixture of Si and SiO_2. Raman spectroscopy results suggests that SiO cannot be considered as a composite mixture of Si and SiO_2.

The amount Si monoxide clusters $(SiO)_n$ was found to be greater for films deposited at high temperature (HT) than the films deposited at room temperature (RT). The provided energy difference between the HT as deposited and the RT as deposited samples was enough for the for the formation of more Si monoxide clusters $(SiO)_n$, while this energy difference was not enough for the genesis of more separate Si since most of the Si-Si bonds are expected to be formed after the formation of Si monoxide clusters $(SiO)_n$. After the formation of Si monoxide clusters $(SiO)_n$, once enough amount of energy provided, clusters can come together and make bond with other clusters and prefer to form Si-Si bonds or Si cores can be formed inside Si oxide clusters and such clusters are expected to lead to nucleation of Si through the combination of small Si suboxide clusters.

A minimum annealing temperature of between 800 and 900^0 C is required to form Si NCs in this kind of a Si-O system. A complete crystallization of amorphous Si was observed at annealing temperature of 1200^0 C.

Results suggest that phase separation and crystallization are two separate processes even at relatively high temperatures.

Investigation on the effect of deposition temperature on post-annealing process suggests that after post-annealing, sample deposited at high temperature (HT, 400^0 C) exhibits an enhanced phase separation than the sample deposited at room temperature (RT) because of the difference between the amount of Si monoxide clusters $(SiO)_n$ at the beginning of post-annealing.

BIBLIOGRAPHY

[1] “Rogers Research Group - University of Illinois.” [Online]. Available: http://rogers.matse.illinois.edu/. [Accessed: 18-Apr-2015].

[2] G. E. Moore, “Cramming more components onto integrated circuits,” *Proc. IEEE*, vol. 86, no. 1, pp. 82–85, 1998.

[3] D. C. Brock, “Understanding Moore’s Law: Four Decades of Innovation,” *Chemical Heritage Press*, 2006.

[4] G. E. Moore, “Progress in digital integrated electronics,” *Int. Electron Devices Meet.*, vol. 21, 1975.

[5] M. Lipson, “Guiding, modulating, and emitting light on Silicon - Challenges and opportunities,” *J. Lightw. Technol.*, vol. 23, no. 12. pp. 4222–4238, 2005.

[6] B. Jalali and S. Fathpour, “Silicon photonics,” *J. Lightw. Technol.*, vol. 24, no. 12. pp. 4600–4615, 2006.

[7] V. R. Almeida, C. A. Barrios, R. R. Panepucci, and M. Lipson, “All-optical control of light on a silicon chip.,” *Nature*, vol. 431, no. 7012, pp. 1081–1084, 2004.

[8] “CMOS board camera / USB - 3.1 Mpix, 2048 x 1536 pix, 12 fps | Lu371 - Lumenera.” [Online]. Available: http://www.directindustry.com/prod/lumenera/cmos-board-cameras-usb-17338-311005.html. [Accessed: 13-May-2015].

[9] J. Perlin, L. Kazmerski, and S. Moon, “Good as gold: the silicon solar cell turns 50.,” *Sol. Today*, vol. 18, no. 1, pp. 24–27, 2004.

[10] “Solar Cells | Allied Scientific Pro.” [Online]. Available: http://alliedscientificpro.com/shop/solar-cells/. [Accessed: 14-Apr-2015].

[11] L. Brus, “Luminescence of silicon materials: chains, sheets, nanocrystals, nanowires, microcrystals, and porous silicon,” *J.Phys.Chem.*, vol. 98, no. 14, Journal; General Review CODEN: JPCHAX; ISSN: 0022–3654, pp. 3575–3581, 1994.

[12] D. M. Holunga, R. C. Flagan, and H. A. Atwater, “A scalable turbulent mixing aerosol reactor for oxide-coated silicon nanoparticles,” *Ind. Eng. Chem. Res.*, vol. 44, no. 16, pp. 6332–6341, 2005.

[13] K. S. Min, K. V Shcheglov, C. M. Yang, H. A. Atwater, M. L. Brongersma, and A. Polman, “Defect-related versus excitonic visible light emission from ion beam synthesized Si nanocrystals in SiO_2,” *Appl. Phys. Lett.*, vol. 69, no. 14, pp. 2033–2035, 1996.

[14] T. Shimizu-Iwayama, N. Kurumado, D. E. Hole, and P. D. Townsend, “Optical properties of silicon nanoclusters fabricated by ion implantation,” *J. Appl. Phys.*, vol. 83, no. 11. pp. 6018–6022, 1998.

[15] M. Hirasawa, T. Orii, and T. Seto, “Size-dependent crystallization of Si nanoparticles” *Appl. Phys. Lett.*, vol. 88, no. 9, pp. 3–6, 2006.

[16] W. S. Cheong, N. M. Hwang, and D. Y. Yoon, “Observation of nanometer silicon clusters in the hot-filament CVD process,” *J. Cryst. Growth*, vol. 204, no. 1, pp. 52–61, 1999.

[17] M. M. Giangregorio, M. Losurdo, G. . Bianco, P. Capezzuto, and G. Bruno, “Nanostructuring Si–C alloys by plasma enhanced chemical vapor deposition: An ellipsometry and Raman spectroscopy investigation,” *Thin Solid Films*, vol. 519, no. 9. pp. 2787–2790, 2011.

[18] N. Tomozeiu, E. E. Van Faassen, W. M. Arnoldbik, A. M. Vredenberg, and F. H. P. M. Habraken, “Structure of sputtered silicon suboxide single- and multi-layers,” in *Thin Solid Films*, 2002, vol. 420–421, pp. 382–385.

[19] U. Kahler and H. Hofmeister, “Visible light emission from Si nanocrystalline composites via reactive evaporation of SiO,” *Opt. Mater. (Amst).*, vol. 17, no. 1–2, pp. 83–86, 2001.

[20] C. W. Jiang and M. A. Green, “Silicon quantum dot superlattices: Modeling of energy bands, densities of states, and mobilities for silicon tandem solar cell applications,” *J. Appl. Phys.*, vol. 99, no. 11, 2006.

[21] Y. Kuwayama, K. Hirose, N. Sata, and Y. Ohishi, “The pyrite-type high-pressure form of silica.,” *Science*, vol. 309, no. 5736, pp. 923–925, 2005.

[22] N. Nishiyama, F. Wakai, H. Ohfuji, Y. Tamenori, H. Murata, T. Taniguchi, M. Matsushita, M. Takahashi, E. Kulik, K. Yoshida, K. Wada, J. Bednarcik, and T. Irifune, “Fracture-induced amorphization of polycrystalline SiO_2 stishovite: a potential platform for toughening in ceramics,” *Sci. Rep.*, vol. 4, p. 6558, 2014.

[23] B. Friede and M. Jansen, “Some comments on so-called ‘silicon monoxide’,” *J. Non. Cryst. Solids*, vol. 204, no. 2, pp. 202–203, 1996.

[24] K. Schulmeister and W. Mader, “TEM investigation on the structure of amorphous silicon monoxide,” *J. Non. Cryst. Solids*, vol. 320, no. 1–3, pp. 143–150, 2003.

[25] G. Moody, “Confinement Effects on the Electronic and Optical Properties of Semiconductor Quantum Dots Revealed with Two-Dimensional Coherent Spectroscopy,” 2013.

[26] E. U. Rafailov, M. A. Cataluna, and E. A. Avrutin, *Ultrafast Lasers Based on Quantum Dot Structures: Physics and Devices*. Wiley, 2011.

[27] A. D. Yoffe, “Low-dimensional systems: quantum size effects and electronic properties of semiconductor microcrystallites (zero-dimensional systems) and some quasi-two-dimensional systems,” *Adv. Phys.*, vol. 42, no. 2, pp. 173–262, 1993.

[28] H. R. Pruppacher, J. D. Klett, and P. K. Wang, “Microphysics of Clouds and Precipitation,” *Aerosol Sci Technol.*, vol. 28, no. 4. pp. 381–382, 1998.

[29] P. G. Debenedetti, *Metastable Liquids Concepts and Principles*. 1996.

[30] R. P. Sear, “Nucleation: theory and applications to protein solutions and colloidal suspensions,” *J. Phys. Condens. Matter*, vol. 19, no. 3. p. 033101, 2007.

[31] H. Henry Teng, “How ions and molecules organize to form crystals,” *Elements*, vol. 9, no. 3, pp. 189–194, 2013.

[32] F. F. ABRAHAM, *Homogeneous Nucleation Theory*. Elsevier, 1974.

[33] M. Nič, “IUPAC Compendium of Chemical Terminology 2nd Edition (1997),” *IUPAC Compend. Chem. Terminol. Gold B.*, vol. 2, pp. 1997–1997, 1997.

[34] W. Ostwald, “Studien uber die Bildung und Umwandlung fester Korper,” *Zeitschrift für Phys. Chemie*, vol. 22, pp. 289–302, 1897.

[35] A. Baldan, “Progress in Ostwald ripening theories and their applications to the precipitates in nickel-base superalloys Part II: Nickel-base superalloys,” *J. Mater. Sci.*, vol. 37, no. 12. pp. 2379–2405, 2002.

[36] I. M. Lifshitz and V. V. Slyozov, “The kinetics of precipitation from supersaturated solid solutions,” *J. Phys. Chem. Solids*, vol. 19, no. 1–2. pp. 35–50, 1961.

[37] C. Wagner, “Theorie der Alterung von Niederschlägen durch Umlösen,” *Zeitschrift für Elektrochemie*, vol. 65, no. 7/8, pp. 581–591, 1961.

[38] C. V. Raman, “A new radiation,” *Proc. Indian Acad. Sci. - Sect. A*, vol. 37, no. 3, pp. 333–341, 1953.

[39] P. Atkins and J. De Paula, “Atkins’ physical chemistry,” in *Chemistry*, 2009, pp. 783–827.

[40] G. Gouadec and P. Colomban, “Raman Spectroscopy of nanomaterials: How spectra relate to disorder, particle size and mechanical properties,” *Prog. Cryst. Growth Charact. Mater.*, vol. 53, pp. 1–56, 2007.

[41] P. Colomban and C. Truong, “Non-destructive Raman study of the glazing technique in lustre potteries and faience(9–14th centuries): silver ions, nanoclusters, microstructure and processing,” *J. Raman Spectrosc.*, vol. 35, no. 3, pp. 195–207, 2004.

[42] C. Smit, R. A. C. M. M. Van Swaaij, H. Donker, A. M. H. N. Petit, W. M. M. Kessels, and M. C. M. Van de Sanden, “Determining the material structure of microcrystalline silicon from Raman spectra,” *J. Appl. Phys.*, vol. 94, no. 5. pp. 3582–3588, 2003.

[43] R. Tsu, J. Gonzalez-Hernandez, S. S. Chao, S. C. Lee, and K. Tanaka, “Critical volume fraction of crystallinity for conductivity percolation in phosphorus-doped Si:F:H alloys,” *Appl. Phys. Lett.*, vol. 40, no. 6, pp. 534–535, 1982.

[44] G. Arfken, “Mathematical Methods for Physicists,” *American Journal of Physics*, vol. 40, no. 4. p. 642, 1972.

[45] S. W. Smith, “Fourier Transform Properties,” in *The Scientist and Engineer’s Guide to Digital Signal Processing*, 1997, pp. 185–208.

[46] N. Jaggi and D. R. Vij, “Fourier transform infrared spectroscopy,” *Handb. Appl. Solid State Spectrosc.*, pp. 411–450, 2006.

[47] J. P. Lee and M. B. Comisarow, “Advantageous apodization functions for magnitude-mode Fourier transform spectroscopy,” *Appl. Spectrosc.*, vol. 41, no. 1, pp. 93–98, 1987.

[48] P. Sutton, *Introduction to Fourier Optics*, vol. 8, no. 5. 1996.

[49] E. Huggins, “Introduction to Fourier Optics,” *The Physics Teacher*, vol. 45, no. 6. p. 364, 2007.

[50] A. Einstein, “Concerning an heuristic point of view toward the emission and transformation of light,” *Am. J. Phys.*, vol. 33, no. 5, p. 367, 1965.

[51] H. Siegbahn and K. Siegbahn, “ESCA applied to liquids,” *J. Electron Spectrosc. Relat. Phenom.*, vol. 2, no. 3. pp. 319–325, 1973.

[52] M. Sasaki and T. Ehara, “Silicon Oxide Thin Films Prepared by Vacuum Evaporation and Sputtering Using Silicon Monoxide,” *J. Phys. Conf. Ser.*, vol. 417, p. 012028, 2013.

[53] R. Zhang, T. Chu, H. Cheung, N. Wang, and S. Lee, “High reactivity of silicon suboxide clusters,” *Phys. Rev. B*, vol. 64, no. 11, pp. 4–7, 2001.

[54] R. Q. Zhang, M. W. Zhao, and S. T. Lee, “Silicon monoxide clusters: The favorable precursors for forming silicon nanostructures,” *Phys. Rev. Lett.*, vol. 93, no. 9, pp. 7–10, 2004.

[55] A. G. Imer, S. Yerci, A. S. Alagoz, M. Kulakci, U. Serincan, T. G. Finstad, and R. Turan, “Evolution of vibrational modes of SiO_2 during the formation of Ge and Si nanocrystals by ion implantation and magnetron sputtering.,” *J. Nanosci. Nanotechnol.*, vol. 10, no. 1. pp. 525–531, 2010.

[56] D. Nesheva, I. Bineva, Z. Levi, Z. Aneva, T. Merdzhanova, and J. C. Pivin, “Composition , structure and annealing-induced phase separation in SiO_x films produced by thermal evaporation of SiO in vacuum,” *Vacuum*, vol. 68, pp. 1–9, 2003.

[57] P. G, Pai, S. S. Chao, Y. Takagi, G. Lucovsky “Infrared spectroscopic study of SiOx films produced by plasma enhanced chemical vapor deposition,” *J. Vac. Sci. Technol., A*, vol. 4, no. 3. pp. 689–694, 1986.

[58] D. Nesheva, C. Raptis, A. Perakis, I. Bineva, Z. Aneva, Z. Levi, S. Alexandrova, and H. Hofmeister, “Raman scattering and photoluminescence from Si nanoparticles in annealed SiO_x thin films,” *J. Appl. Phys.*, vol. 92, no. 8, pp. 4678–4683, 2002.

[59] A. Wellner, V. Paillard, C. Bonafos, H. Coffin, A. Claverie, B. Schmidt, and K. H. Heinig, “Stress measurements of germanium nanocrystals embedded in silicon oxide,” *J. Appl. Phys.*, vol. 94, no. 9, pp. 5639–5642, 2003.

[60] “Moore’s Law is dead, long live Moore’s Law | ExtremeTech.” [Online]. Available: http://www.extremetech.com/extreme/203490-moores-law-is-dead-long-live-moores-law. [Accessed: 31-May-2015].